Heave and Pitch Motions of Wing-in-Ground Craft Flying above Wavy Surface

Konstantin I. Matveev

School of Mechanical and Materials Engineering, Washington State University, Pullman, WA, 99164-2920, USA

matveev@wsu.edu

Abstract

Wing-in-ground (WIG) craft can take advantage of increased aerodynamic lift and reduced drag when flying in a proximity to a water or ground surface. Dynamics of the vehicles flying in ground effect is more complex due to a strong sensitivity to the flight height. Heave and pitch motions of a WIG craft are analyzed in this study considering lift forces generated on a main wing flying in strong ground effect and a smaller tail wing operating out of ground effect. A potential flow theory is applied for modeling the unsteady pressure distribution under the main wing. The effect of the tail wing on the vehicle stability is demonstrated in a flight over a flat surface. Heave-pitch motions are simulated for flights over wavy surfaces in a range of amplitudes and lengths of surface waves.

Keywords

Ground Effect Aerodynamics; Stability; Heave-Pitch Motions; Potential Flow Theory

Introduction

Wing-in-ground (WIG) craft are high-speed marine vehicles that fly in the proximity to the water or ground surface [1]. The aerodynamic lift in such flying regimes can be substantially increased due to higher pressure on the wing lower side, while the induced drag generally decreases due to partial blockage of tip vortices by the underlying surface. The propulsion systems can also be affected by the ground vicinity [2]. WIG craft are considered as promising transportation means for applications that require either higher speeds than those of fast boats or larger payloads than aircraft can carry.

A variety of prototype WIG craft have been built, but their broad application has not occurred. One of the main barriers is more complex dynamics due to ground effect on the vehicle aerodynamics, as well as safety concerns due to high-speed motion near water/ground surface [3]. This study aims at modeling heave and pitch motions of a WIG craft. A simplified WIG configuration, shown in Fig. 1, is considered here with the finite-span main wing operating in the so-called extreme ground effect, when the distance between ground and wing is much smaller than the wing chord and the lift increase is especially significant. A stabilizing tail is utilized, since most airfoil profiles tend to be unstable in ground-effect flight. The present study is built upon our previous models [4,5] that considered an infinite-span wing (practically unrealistic) and a tailless setup with an S-shaped airfoil that has lower aerodynamic performance for the sake of improved stability properties.
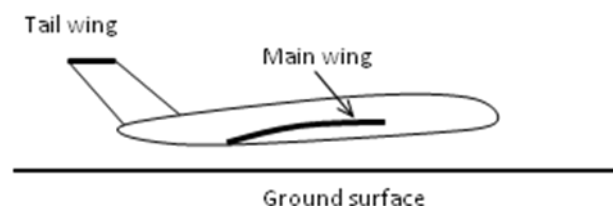

FIG. 1 SCHEMATIC OF WIG CRAFT

Mathematical Model

A wing with a small attack angle moving steadily over a wavy surface is considered (Fig. 2). The distance between the wing and the surface is assumed to be much smaller than the wing chord. In this situation, known as the "extreme" ground effect (EGE) flow, the dominant lift component is generated on the lower side of the wing, and

the flow under the wing becomes nearly two-dimensional (in x- and z-directions). The influence of the flow in the wake and above the wing on the under-wing flow is ignored. A possible but computationally expensive approach to model WIG flow can involve detailed simulations with CFD methods [6]. In the present study, however, viscous effects are neglected and computationally efficient potential flow theory is utilized. The governing equation for the unsteady perturbed velocity potential φ in the channel under the wing can be expressed as follows [1],

$$\frac{\partial}{\partial x}\left(h\frac{\partial \varphi}{\partial x}\right)+\frac{\partial}{\partial z}\left(h\frac{\partial \varphi}{\partial z}\right)=U\frac{\partial h}{\partial x}-\frac{\partial h}{\partial t},\tag{1}$$

where h is the local channel height and U is the wing forward speed (or the velocity of the incident flow in the reference frame moving with the wing). In the extreme ground effect, the appropriate boundary conditions are $\varphi=0$ at the wing leading edge and zero gage pressure on the wing side and trailing edges, which results in the following requirement [1],

$$2U\frac{\partial \varphi}{\partial x}-2\frac{\partial \varphi}{\partial t}-\left(\frac{\partial \varphi}{\partial x}\right)^2-\left(\frac{\partial \varphi}{\partial z}\right)^2=0.\tag{2}$$
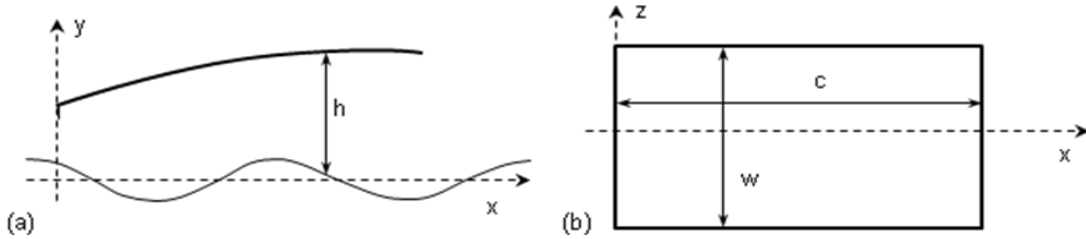

FIG. 2 (a) SIDE AND (b) TOP VIEW OF A MAIN WING

In this study, only heave and pitch motions are considered. Given the forward speed, wing geometry on the lower side, wing kinematics, and the surface deformations, Eqs. (1-2) can be solved numerically to determine the velocity potential. The second-order finite difference scheme in space and the first order implicit finite difference scheme in time domain are employed in this study. To achieve mesh-independence, the spatial and time steps should be selected as $\Delta x=c/20$ and $\Delta t=\Delta x/2U$, where c is the wing chord [7]. Upon finding the velocity potential the gage pressure on the wing lower side can be computed with help of the unsteady Bernoulli equation,

$$p=\rho\left[U\frac{\partial \varphi}{\partial x}-\frac{\partial \varphi}{\partial t}-\frac{1}{2}\left(\frac{\partial \varphi}{\partial x}\right)^2-\frac{1}{2}\left(\frac{\partial \varphi}{\partial z}\right)^2\right],\tag{3}$$

where ρ is the air density. Then, the force on the lower side of the main wing F_w and the center of pressure x_w is determined by integrating this pressure over the wing planform.

In addition to the main wing flying in ground effect, we consider a tail wing operating out of ground effect, which is employed for the purpose of stabilizing. The tail is assumed to be positioned far above the main wing and ground to neglect their influence of the tail wing aerodynamics. The tail wing lift is modeled here in the quasi-steady approximation as that of a flat wing with chord c_t and aspect ratio λ_t,

$$F_t=\frac{2\pi \alpha_t}{1+2/\lambda_t}\frac{1}{2}\rho U^2 c_t,\tag{4}$$

where α_t is the effective attack angle affected by the vehicle kinematics,

$$\alpha_t=\alpha_{t0}+\alpha-\frac{\dot{y}_{cg}}{U}+\frac{\dot{\alpha}(x_{cg}-x_t)}{U},\tag{5}$$

where α_{t0} is the installed attack angle of the tail wing with respect to the main wing, α is the attack angle of the main wing, $\dot{y}_{cg}$ is the vertical velocity of the vehicle center of gravity, and x_{cg} and x_t are the horizontal positions of the center of gravity and the tail wing lift force application, respectively.

Dynamics of a WIG craft with only two degrees of freedom (heave and pitch) is analyzed in this study. Only main aerodynamic lifting forces on the main wing and tail are accounted, in addition to the vehicle weight. The lift force components on the fuselage and the upper wing surface are neglected in line with the extreme ground-effect theory. The drag and thrust contributions to the pitch moment are also ignored. Hence, the governing dynamic equations can be written as follows,

$$M\,\ddot{y}_{cg} = F_w + F_t - Mg\ , \tag{6}$$

$$I\,\ddot{\alpha} = F_w(x_w - x_{cg}) + F_t(x_t - x_{cg})\ , \tag{7}$$

where M and I are the mass and the moment of inertia of a WIG craft, respectively, and g is the gravitational acceleration. Starting with given initial conditions and numerically integrating the dynamics equations (Eqs. 6-7) together with equations for the velocity potential (Eqs. 1-3) and the tail wing forces (Eqs. 4-5), one can simulate the vertical-plane trajectory of the vehicle.

Results

First, results of the EGE theory for the pressure distribution under a ram wing are compared here with wind-tunnel measurements carried out by Gallington and Miller [8] on a small-scale model with aspect ratio of 2/3. The setup schematic and data are shown in Fig. 3. A reasonable agreement is observed, noting unknown experimental uncertainties and visous effects that might be important in tests with small-scale setups. Rozhdestvensky [1] has also found a good agreement between theoretical and test results for a flat plate of aspect ratio 1 mounted above the flat surface at small relative clearances.
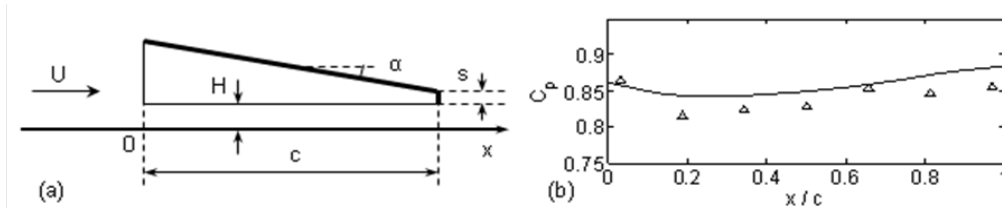

FIG. 3 (a) EXPERIMENTAL RAM WING SETUP. (b) PRESSURE COEFFICIENT AT THE CENTERLINE. TRAINGLES, TEST DATA; CURVE, MODELING RESULTS. s/c = 0.017, α = 5.7°, H/c = 0.033.

The mathematical model described above is applied here for simulating heave-pitch motions of one WIG configuration with the following non-dimensional characteristics: mass coefficient $\mu = \dfrac{2M}{\rho w c^2} = 4$ (where w is the main wing span), the moment of inertia coefficient $i = \dfrac{I}{Mc^2} = 0.1$, the center of gravity location $\dfrac{x_{cg}}{c} = 0.54$, the main wing aspect ratio $\dfrac{w}{c} = 1$, and the Froude number of the equilibrium flight $Fr = \dfrac{U}{\sqrt{gc}} = 4.0$. The main wing has a parabolic profile with the relative camber of 0.01. The tail wing has the following parameters: the relative chord $\dfrac{c_t}{c} = 0.2$, aspect ratio $\lambda_t = 6$, installed attack angle $\alpha_{t0} = -3.5°$, and the position of the center of pressure $\dfrac{x_t}{c} = -0.3$.

In the equilibrium flight over a flat (no waves) surface, the attack angle of the main wing is $\alpha = 3.5°$ (so that the tail wing has the zero-lift angle) and the relative distance from the trailing edge of the main wing to the ground surface is $\dfrac{h_{TE}}{c} = 0.035$. It should be noted that it is not a requirement for the tail wing to produce zero vertical force in equilirbirum flying regimes; this wing can be installed at other angles.

The first set of calculations demonstrates the importance of the tail wing to ensure the vehicle longitudinal stability. Simulations have been conducted for dynamics of a WIG craft with and without tail wing in the flight over a flat surface with a small initial deviation from the equilibrium. Results for pitch and heave parameters are shown in Fig. 4, where symbols with subscript 0 correspond to the equilibrium state. As one can see, the tailless setup is unstable. Despite the initial motions towards the equilibrium, the vehicle eventually pitches down. If no action is taken by a pilot, it will collide with the underlying surface. On the other hand, the configuration with the tail is

stable. Upon the initial deviation, oscillatory heave and pitch motions die out, and the vehicle returns to the equilibrium state.
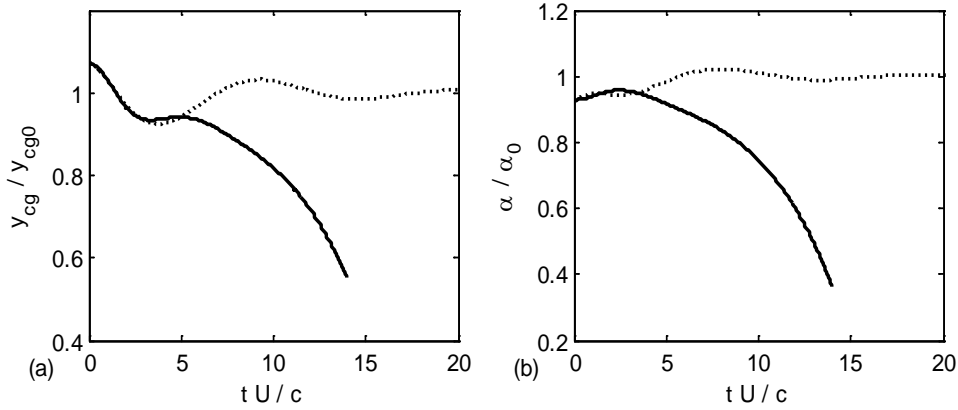

FIG. 4 (a) HEAVE AND (b) PITCH MOTIONS AFTER INITIAL DEVIATION. SOLID LINE, TAILLESS SETUP; DOTTED LINE, WITH TAIL STABILIZER.

Since WIG craft are usually designed to fly over water surfaces at relatively small clearances, it is important to understand its motions caused by the surface non-uniformities such as waves. Here, we consider sinusoidal surface waves, as schematically indicated in Fig. 2a. The unsteady motions of the same WIG setup have been simulated first over a range of wavelength λ and a constant relative wave height $A_w / c = 0.005$, which corresponds to nearly linear dynamics. The amplitudes of heave and pitch motions of a WIG craft in a steady state normalized by the amplitude and maximum slope of the surface waves are shown in Fig. 5. The amplitudes are defined as the half-difference between the maximum and minimum values of kinematic parameters over a period of limit-cycle oscillations,

$$y_1 = (\max(y_{cg}) - \min(y_{cg})) / 2 ,$$ (8)

$$\alpha_1 = (\max(\alpha) - \min(\alpha)) / 2 .$$ (9)

When the waves are very short, the vehicle does not have time to react to these disturbances, so the heave and pitch motions are very small (Fig. 5). In the limit of very long waves, the vehicle follows the wave contour, so the relative responses approach one as expected. There is a certain value of the surface wavelength at which the heave and pitch motions reach maximal values. For the considered here WIG setup, this resonance occurs when $\lambda_w / c \approx 11$. In this situation, the corresponding frequency of encounter coincides with the natural frequency of the WIG dynamical system. Motions at the resonance should be avoided since the amplitudes may reach dangerous values leading to a collision with the underlying surface. This can be accomplished, for example, by altering flying attitude (trim/height) or relative speed.
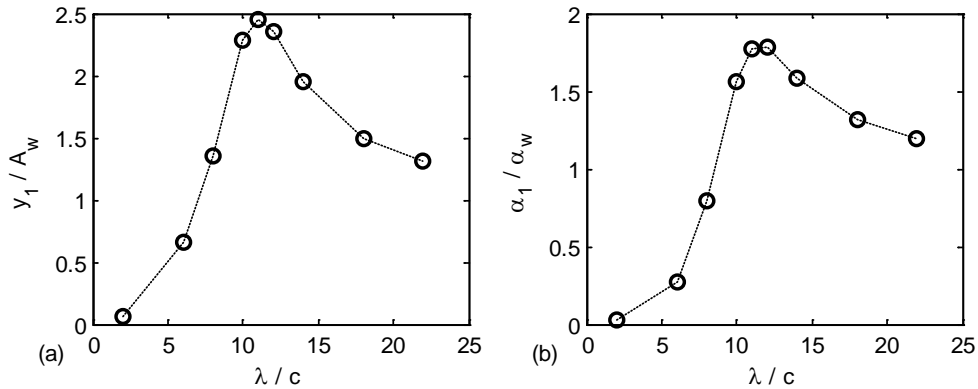

FIG. 5 AMPLITUDES OF (a) HEAVE AND (b) PITCH MOTIONS OF A WIG CRAFT FLYING ABOVE SURFACE WAVES WITH VARIABLE LENGTH

The proximity to the ground and strong ground effect cause significant nonlinearity of the WIG system dynamics, so that linear analysis cannot be used even for moderate motions in practical situations. In these cases, a

dependence of motions on the disturbance amplitude must be assessed. Another set of calculations has been done for a range of wave amplitudes near the linear resonance state ($\lambda_w / c = 11$). The relative responses in steady-state cycles are plotted in Fig. 6. As one can see, the relative responses actually decrease with the increase of disturbances (although their absolute values naturally increase). Hence, in the considered system, the nonlinearity provides additional dampening of heave-pitch motions. However, this result may be specific to the configuration and operational conditions considered in this study and cannot be directly generalized to other situations.
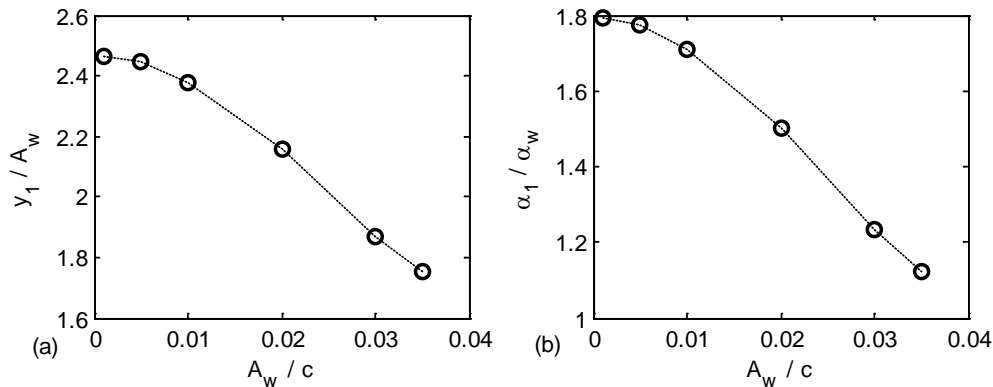

FIG. 6 AMPLITUDES OF (a) HEAVE AND (b) PITCH MOTIONS OF A WIG CRAFT FLYING ABOVE SURFACE WAVES WITH VARIABLE HEIGHT

Conclusions

A simplified dynamical system has been applied in this study to analyze dynamics of a WIG craft with the main wing in strong ground effect and a tail wing out of ground effect. It was demonstrated that the tail wing provides a stabilizing influence. When moving above wavy surfaces, the considered WIG configuration showed heave-pitch responses resembling those of a damped oscillator with a potentially dangerous resonance condition occurring at a certain wavelength of the surface non-uniformity. It was also found that the increase of disturbances leads to the reduction of normalized motions. The future extensions of this study may include investigating the effect of the tail size on WIG craft motions, transient flying regimes, other disturbance scenarios, and adding more degrees of freedom to the vehicle.

REFERENCES

[1] Rozhdestvensky, K.V. Aerodynamics of a Lifting System in Extreme Ground Effect. Heidelberg: Springer-Verlag, 2000.

[2] Iboshi, N., Itoga, N., Prasad, J.V.D., and Sankar, L.N. "Ground Effect of a Rotor Hovering above a Confined Area." Frontiers in Aerospace Engineering 3 (2014): 7-16.

[3] Matveev, K.I. and Kornev, N. "Dynamics and Stability of Boats with Aerodynamic Support." Journal of Ship Production and Design 29 (2013): 17-24.

[4] Matveev, K.I. "Heave-Pitch Motions of a Platform Flying in Extreme Ground Effect." Journal of Aerospace Engineering 25 (2012): 238-245.

[5] Matveev, K.I. "Unsteady Motions of a Ram Wing Flying above Waves and Low-Height Obstacles." Proceedings of the 31st AIAA Applied Aerodynamics Conference, San Diego, CA, 2013.

[6] Bagade, P.M., Krishnan, S.B., and Sengupta, T.K. "DNS of Low Reynolds Number Aerodynamics in the Presence of Free Stream Turbulence." Frontiers in Aerospace Engineering 4 (2015): 20-34.

[7] Matveev, K.I. "Modeling of Finite-Span Ram Wings Moving above Water at Finite Froude Numbers." Journal of Ship Research 58 (2014): 146-156.

[8] Gallington, R.W. and Miller, M.K. "The Ram-Wing: a Comparison of Simple One-Dimensional Theory with Wind Tunnel and Free Flight Results." Proceedings of the AIAA Guidance, Control and Flight Mechancis Conference, Santa Barbara, CA, 1970.

Konstantin I. Matveev is an Associate Professor in the School of Mechanical and Materials Engineering at Washington State University. He received B.S. and M.S. degrees in Applied Physics from Moscow Institute of Physics and Technology. He obtained a Ph.D. degree in Mechanical Engineering at California Institute of Technology in 2003. As a post-doc, Dr. Matveev carried out research at Los Alamos National Laboratory. Then, he worked as a Senior Hydrodynamicist for Art Anderson Associates in Bremerton. Dr. Matveev participated in research and development of high-performance marine vehicles, including low-drag air-cavity hulls, fast amphibious platforms, and multi-hull ships. In 2006, Dr. Matveev joined Washington State University, where he established a research group specializing in advanced marine and aerial craft and energy conversion systems. He published over 50 journal articles and co-authored a book on small-waterplane-area ships.

Research of Characteristics of Isentropic Air Intake and Ducted Isentropic Air Intake

Zvegintsev V.I.[1], Safonov V.A.[2]

[1]Chief scientist, Khristianovich Institute of Theoretical and Applied Mechanics Siberian Branch of Russian Academy of Sciences, Novosibirsk, Institutskaya str., 4/1, 630090, Russia

[2]Student, Novosibirsk State University, Novosibirsk, Pirogova str., 2, 630090, Russia

[1]zvegin@itam.nsc.ru; [2]vitalysaf@gmail.com

Abstract

The characteristics of hypersonic air intake with isentropic compression are investigated by numerical simulation of viscous and inviscid flow in this article. Software ANSYS Fluent are used for modeling the flow. The results are presented as numerical values of characteristics of studied hypersonic isentropic air intake. It is shown that the boundary layer significantly modifies the characteristics of the flow in the throat of air intake.

Keywords

Isentropic Air Intake, Hypersonic Air Intake, Ducted Air Intake

Introduction

Supersonic and hypersonic air intakes in the air-jet engines are designed to enhance the static gas pressure by reducing its kinetic energy during braking in system of nonisentropic shock waves. In the 70s in the ITAM SB RAS it was proposed to use flow with isentropic compression to build hypersonic air intakes. For example in [1], experiments were conducted with high Mach number (M=11.5). It was carried out flow around the air intake with the section of isentropic compression at the different angles of attack. In [2] it was conducted a general analysis of the characteristics of the convergent air intake.

In [3] analysis of the characteristics of three-dimensional air intake Busemann (Eng. Busemann) for M = 6.0 was carried out. Results of this work show how to change the basic parameters of the flow inside the air intake when the angle of the incoming flow is changed.

All the above-mentioned theoretical and computational works were carried out without taking into account the effect of the boundary layer.

In this paper numerical simulation of hypersonic flow around the air intake with the surface of isentropic compression is carried out. It discussed different geometries of air intakes with different parameters of the incident flow. To evaluate the impact of boundary layer which arises on the surface of isentropic compression it compared flows with options of viscous and inviscid flows.

Method of Calculation and Parameters of Modeling

Simulation of the flow around hypersonic air intake with the surface of the gas stream isentropic compression is conducted in software product ANSYS Fluent 14.5. Selected program performs iterations that are performed by the implicit scheme Roe-FDS (Flux difference splitter). Detailed description of the implicit scheme Roe-FDS is given in [4].

In the simulation with using ANSYS Fluent, iterations are carried out, which resulted in a stationary solution in which the domain is set. Control of stationarity of solution is conducted by analyzing the value of Mach number at each point. In the region where the values in the neighboring cells are different by more than 0.1%, it produced splitting grid.

Hypersonic Air Intake with Isentropic Compression Surface

Figure 1 shows a cross-section of a flat air intake for which the calculations in software ANSYS Fluent were carried out. Isentropic compression surface is constructed by the method of the characteristics for an initial M=3. Simulation of flow is carreid out for incoming flow M=3, M=5 and M=7 with flow parameters corresponding altitudes H=0 km, H=10 km, H=30 km. The incoming flow has parameters P=101300 Pa, T=228 K (H=0 km), P=26400 Pa, T=223 K (H=10 km) and P=1200 Pa, T=230 K (H=30 km).
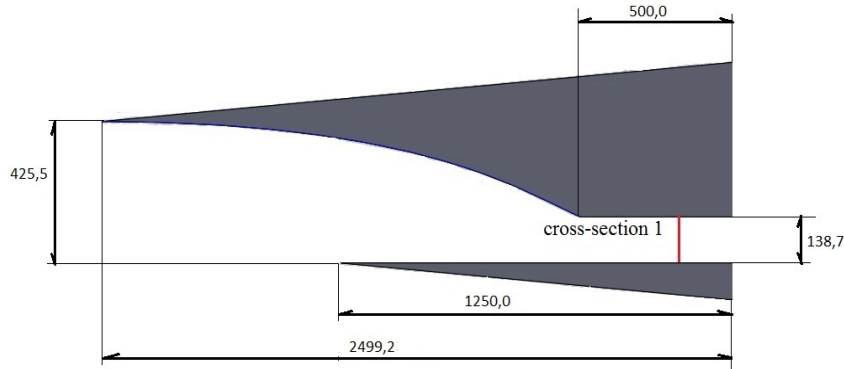
FIG. 1 AIR INTAKE WITH ISENTROPIC COMPRESSION SURFACE

Table 1 shows the values of Reynolds number (for L=1 m) for parameters of flow listed above.

$$\mathrm{Re} = \frac{\rho \upsilon L}{\eta}$$

TABLE 1. VALUES OF REYNOLDS NUMBER (1/M)

Height, km	M=3	M=5	M=7
H=0	$68,8*10^6$	$114,6*10^6$	$160,5*10^6$
H=10	$25,1*10^6$	$41,8*10^6$	$58,6*10^6$
H=30	$1,1*10^6$	$1,9*10^6$	$2,6*10^6$

The Reynolds number is $1,1*10^6$ to $1.6*10^8$ in different initial parameters of the incoming flow. It means that boundary layer can be considered turbulet at all distance of body and we can do not consider the laminar-turbulent transition of flow at the beginning of air intake.

Using the Navier-Stokes equations for a continuum is acceptable for this simulation because Knudsen number for parameters of calculation is smaller than 10^{-3} (see table 2) and that allows to consider the medium as a solid at low altitudes and at high.

$$Kn = 1,483 \frac{M}{\mathrm{Re}}$$

TABLE 2. VALUES OF KNUDSEN NUMBER

Height, km	Knudsen number [1/m]
H=0	$2,4*10^{-6}$
H=10	$6,6*10^{-6}$
H=30	$1,5*10^{-4}$

As a value for analyzing the results the ratio of total pressure recovery σ was selected – the ratio of the avaraged total pressure in the throat of air intake to the total pressure of the incoming flow was selected. The calculation of the total pressure in the throat was carried out for cross-section 1 (see fig. 1) at the distance of 100 mm from the break point of isentropic compression surface inside the throat of the air intake. Averaging of the total pressure was carried out by cross-sectional area of the channel.

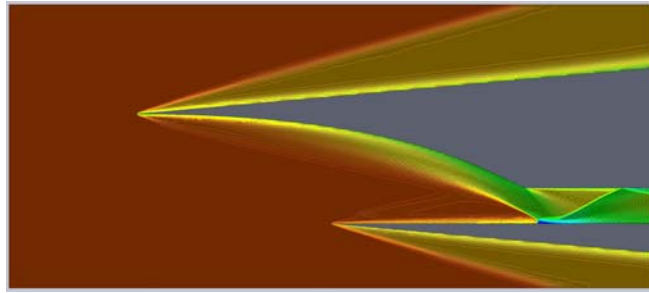Typical distribution of the Mach number in the computational domain is shown in Figure 2.

FIG. 2 EXAMPLE OF MACH NUMBER DISTRIBUTION AROUND THE AIR INTAKE WITH ISENTROPIC COMPRESSION SURFACE IN TRANSVERSE CROSS-SECTION FOR THE PARAMETERS OF THE INCOMING FLOW H=0 KM AND M=5

The values of the ratio of total pressure recovery as a function of the Mach number of the incoming flow are shown in Figures 3-5.
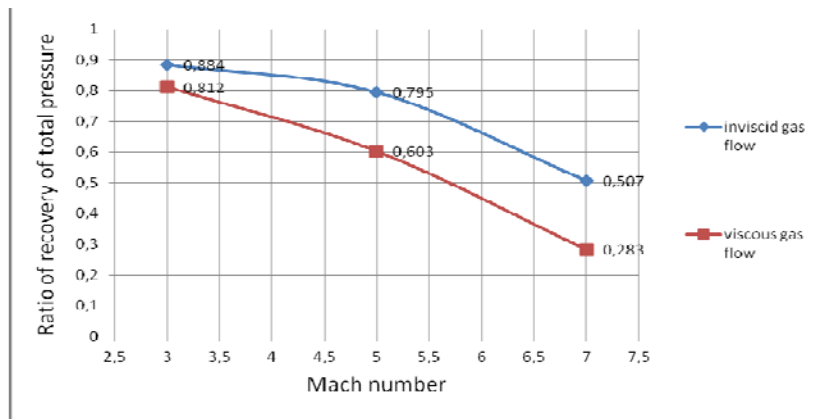

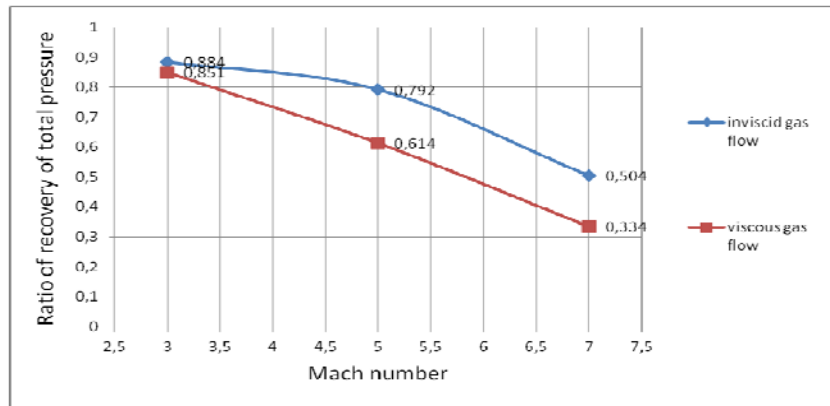FIG. 3 THE DEPENDENCE OF Σ VS THE MACH NUMBER AT THE HEIGHT H=0 KM

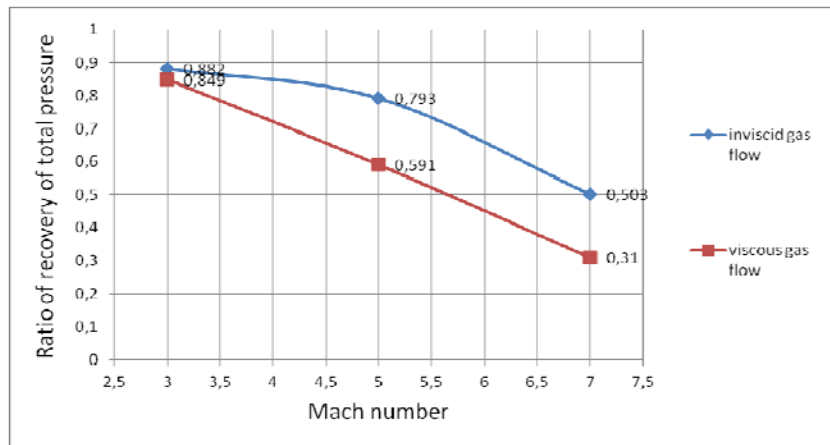FIG. 4 THE DEPENDENCE OF Σ VS THE MACH NUMBER AT THE HEIGHT H=10 KM

FIG. 5 THE DEPENDENCE OF Σ VS THE MACH NUMBER AT THE HEIGHT H=30 KM

In the case of viscous flow, the ratio of total pressure recovery for M=3 is from 97% (H=30 km) to 94% (H=0 km) of the ratio of total pressure recovery in the case of inviscid flow. In the case of viscous flow, the ratio of total pressure recovery for M=7 is 67% (H=30 km) to 43% (H=0 km) of the ratio of total pressure recovery in the case of inviscid flow. Static pressure increased by 56% (H=0 km), 53% (H=10 km) and 34% (H=30 km) in the throat of air intake in the case of viscous flow as compared with the case of inviscid flow. Other basic characteristics of air intake (Mach number, density) are not changed in transition from the case of inviscid flow to the case of viscous flow.

Hypersonic Ducted Air Intake with Isentropic Compression Surface

For placing air intake on the surface of body of aircraft, ducted air intakes are used which have not any elements extending beyond the dimensions of the body. In general, that air intake should direct air flow inside the body of the aircraft where air flow would be deceleration through the shock waves. As a variant of ducted air intake, it can be considered a rotation of air flow by angle θ (see fig. 6). In this ducted air intake, the flow is directed into the body by a rarefaction wave 1 (see fig. 6) and then the flow is decelerated by shock wave 2 (see fig. 6). To obtain a compression wave 2 (see fig. 6) corresponding braking surface is constructed, which is located after the corner point and is based on the method of characteristics for a flow velocity obtained after the turn of the flow in the rarefaction wave 1 (see fig. 6).
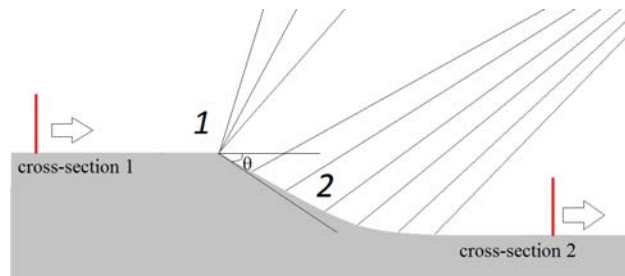

FIG. 6 REPRESENTATION OF THE REVERSAL OF FLOW INSIDE THE BODY

A scheme shown in fig. 6 was designed using the software ANSYS Fluent. Isentropic compression surface was designed for M=3. After the rarefaction, wave 1 corresponds the free-stream with M=2.75 with turning on the external angle of 5°. Typical distribution of Mach number in computational domain is shown in figure 7.
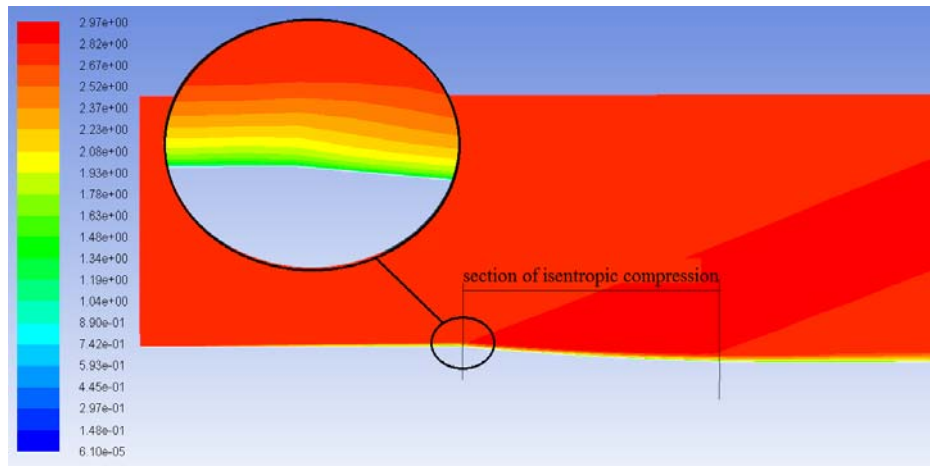

FIG. 7 EXAMPLE OF MACH NUMBER DISTRIBUTION AROUND THE ISENTROPIC COMPRESSION SURFACE OF DUCTED AIR INTAKE IN TRANSVERSE CROSS-SECTION FOR THE PARAMETERS OF THE INCOMING FLOW H=0 KM AND M=2.75

As a value for analyzing the results, the ratio of total pressure recovery was selected. Analysis of the results was performed for cross-section 1 and cross-section 2 (see fig. 6).

The ratio of total pressure recovery is σ=0,999 for the case of inviscid flow. Total pressure loss in the case of a viscous gas flow is result of the formation of the boundary layer that starts to grow up to 1000 mm before the isentropic compression surface. The ratio of total pressure recovery is σ=0,957 for the case of viscous flow with the impact of the boundary layer.

A hypersonic ducted air intake with an isentropic compression surface is presented at figure 8. External angle of rotation is θ=5°. Isentropic compression surface is constructed by the method of characteristics for a Mach number of incoming flow M=3. In addition to the calculated M=3 (M=2.75 incoming flow), underexpanded cases with M=5 and M=7, which correspond to M=4.5 and M=6.15 in front of the rarefaction wave, respectively, are considered.
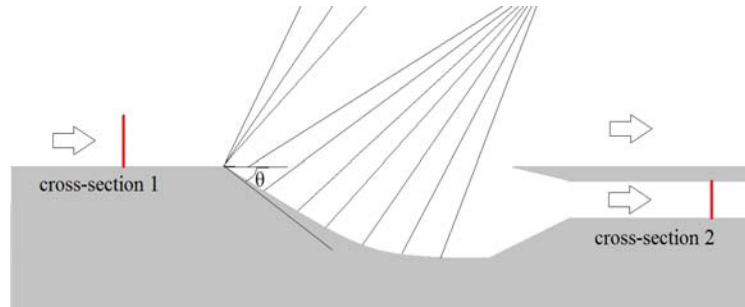

FIG. 8 DUCTED AIR INTAKE WITH AN ISENTROPIC COMPRESSION SURFACE

Numerical modeling of flow is carried out on a incoming flow M=3, M=5 and M=7 with flow parameters relevant H=0 km. Table 3 shows the values of Reynolds number (for L=1 m).

TABLE 3. VALUES OF REYNOLDS NUMBER (1/M)

M of incoming flow	Reynolds number [1/m]
M=2,75	$64,3*10^6$
M=4,5	$105,2*10^6$
M=6,15	$143,8*10^6$

Using the Navier-Stokes equations for a continuum is acceptable for this simulation because Knudsen number for parameters of calculation is $Kn\sim10^{-4}$ and that allows to consider the medium as continious at low altitudes and at high.

The longitudinal lenght of isentropic compression surface is L=484,2 мм. Height of air intake throat is d=17,9 мм.

The calculation of the total pressure of incoming flow is carried out for cross-section 1 (see fig. 8) at a distance of 50 mm from the beginning of the isentropic compression surface. The calculation of the total pressure in the throat is carried out for cross-section 2 (see fig. 8) at a distance of 500 mm from the break point of isentropic compression surface inside the channel of air intake. Averaging of the total pressure in the section 1 is carried out on an area equal to the area of cross-section 2.

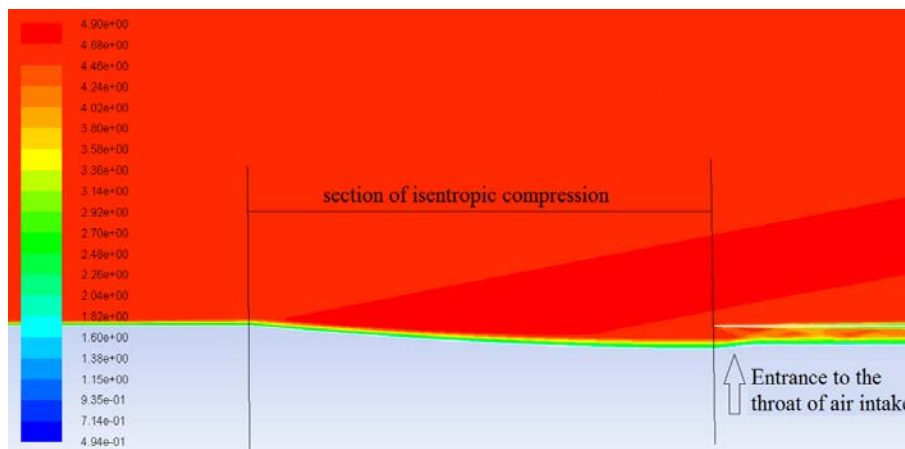Typical distribution of Mach number in computational domain is shown in figure 9.

FIG. 9. EXAMPLE OF MACH NUMBER DISTRIBUTION AROUND THE DUCTED AIR IN TRANSVERSE CROSS-SECTION FOR THE PARAMETERS OF THE INCOMING FLOW H=0 KM AND M=4.5

Values of the ratio of total pressure recovery for case of ducted hypersonic air intake with isentropic compression surface are shown in figure 10.
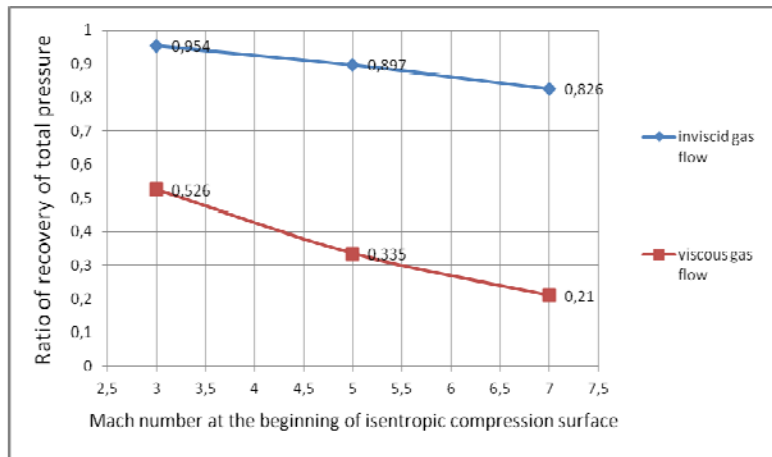
FIG. 10 THE DEPENDENCE OF Σ VS THE MACH NUMBER AT THE HEIGHT H=0 KM

The ratio of total pressure recovery in case of viscous flow is 55% (H=0 km) from value in the case of inviscid flow at M=3 on the isentropic compression surface in air intake with an isentropic compression surface. Values of ratio of recovery of total pressure in the case of viscous flow are 37% and 25% from values in the case of inviscid flow at M=5 and M=7 respectively.

Conclusions

In the case of a hypersonic air intake with isentropic compression surface, the ratio of total pressure recovery in the case of viscous flow for M=3 is 97% (H=30 km) to 94% (H=0 km) of value of the ratio of total pressure recovery in the case of inviscid flow. In the case of viscous flow, ratio of recovery of total pressure for M=7 is 67% (H=30 km) to 57% (H=0 km) of ratio of recovery of total pressure in the case of inviscid flow. Static pressure increased by 56% (H=0 km), 53% (H=10 km) and 34% (H=30 km) in the throat of air intake in the case of viscous flow as compared with the case of inviscid flow. Other basic characteristics of air intake (Mach number, density) are not changed in transition from the case of inviscid flow to the case of viscous flow.

The ratio of total pressure recovery in case of viscous flow is 55% (H=0 km) from value in the case of inviscid flow at M=3 on the isentropic compression surface in ducted air intake with an isentropic compression surface. Values of the ratio of total pressure recovery in the case of viscous flow are 37% and 25% from values in the case of inviscid flow at M=5 and M=7 respectively.

REFERENCES

[1] A.M. Blokhin, L.M. Vetlutskaya, B.I. Gutov, V.N. Dolgov, V.V. Zatoloka, V.V. Shumsky «Convergent input diffusers and axisymmetric supersonic conical Busemann flows», Collection of scientific papers «Aerophysical researches», ITAM SB RAS, Novosibirsk, Russia, 1972.

[2] B.I. Gutov, V.V. Zatoloka, «Convergent input diffusers with the initial compression shock and additional external compression», Collection of scientific papers «Aerophysical researches», ITAM SB RAS, Novosibirsk, Russia, 1974.

[3] V. Ramasubramanian, R. Starkey, M. Lewis, «Numerical Simulations of Busemann Hypersonic Inlets At Finite Flight Angles», AIAA Papers 2008-7497, 2008 p.

[4] H. Deconinck, P. L. Roe, R. Struus, «A multidimensional generalization of Roe's flux difference splitter for the euler equations», Computers Fluids Vol. 22, No. 2/3, pp. 215-222, 1993.

[5] V.V. Ushakov, «Analysis of flow with flow separation around bodies in the SolidWorks/FloWorks», Information and analytical journal «CAD/CAM/CAE Observer» №3(12), 2003.

[6] G. Schlichting, "Boundary layer theory", New-York MacGraw-Hill, p. 817, 1960.

[7] V.I. Zvegintsev, V.A. Safonov, «Research of characteristics of a hypersonic isentropic air intake», Russian Scientific Conference of Physics Students 20, page 500, 2014.

[8]   Vinayagamurthy G, Parammasivam K M, «Flutter Analysis of a Space Vehicle», Frontiers in Aerospace Engineering Volume 3 Issue 3, August 2014.

[9]   P.M. Badage, S.B. Krishnan, T.K. Sengupfa, «DNS of Low Reynolds Number Aerodynamics in the Presence of Free Stream Turbulence», Frontiers in Aerospace Engineering Volume 4 No 1, May 2015.

Professor V. Zvegintsev is well-known specialist in the field of experimental aerodynamics. He is the designer of new type short-duration wind tunnels, which are of interest over the world. He has published more than 150 scientific papers and his monograph "Short-duration gas-dynamic facilities. P.1. Facilities for scientific research" is among them. The scope of his current interests concerns the experimental investigations of hypersonic vehicles with air-breathing propulsion with help of short-duration gasdynamic facilities.

V. Safonov is a student of Department of Aerophysics and Gaseous Dynamics Physics Faculty of Novosibirsk State University. Since 2011 he has been studying isentropic surface of compression. The scope of his current interests is a studing of air intake with isentropic surface of compression with taking into account the boundary layer of viscous gas.

Dynamic Response of Nanocomposite Laminates During Low, Medium and High Velocity Impact Loading

G. Balaganesan[*1], R. Velmurugan[2], K. Kanny[2]

[1,2]Department of Aerospace Engineering, Indian Institute of Technology Madras, India

[1,2]Department of Mechanical Engineering, Durban University of Technology, Durban, South Africa

[*1]gbganesh@iitm.ac.in; [2]ramanv@iitm.ac.in; [3]kkanny@dut.ac.za

Abstract

The composite laminates are subjected to impact loading in various conditions with different energy levels. The energy levels are varied by varying mass and speed of the striking mass. The conditions are low velocity of impact with heavy mass, light mass projectile with medium and high velocity of impact. The impact due to bullet is considered as light mass with high velocity of impact. Dynamic response of nanocomposite laminates in drop mass test and projectile impact is studied for low velocity impact. The acceleration and time duration of vibration are found experimentally for the glass/epoxy laminates with and without nano fillers. The values of peak acceleration and period of vibration are compared for the laminates of different thicknesses and percentage of filler dispersion. The damping factor values are predicted for low velocity impact loading by logarithmic decrement method and by FFT spectrum analysis for medium and high velocity impact.

Keywords

Nanocomposites; Impact Loading; Dynamic Response; Acceleration; Vibration; Damping

Introduction

It is essential to design of structures for minimum noise and vibration. The information on damping coefficients of structural materials is also essential for dissipation of energy during vibration of a structure [1]. Experimental and analytical characterization of damping is not easy, even for conventional structural materials, and the anisotropic nature of composite materials makes it even more difficult [2-3]. A structure can be made to vibrate with excessive, sustained, oscillatory motion during the operation of a system. Resonant vibration is caused by an interaction between the inertial and elastic properties of the materials within the structure. Resonant vibration is often the cause of, or at least a contributing factor to many of the vibration related problems that occur in structures and operating machinery. For better understanding of any structural vibration problem the resonances of a structure needs to be identified and quantified [4-5]. Vibration modes are used as a simple and efficient mean of characterizing resonant vibration. A common way of doing this is to define the structure's modal parameters natural frequency and damping factor. The flexural damping capacity of the composite laminates is due to the material properties, the ply orientation and the stacking sequences of the layers [6-8]. In the past, there were several works on analytical models to predict the damping responses of composite laminates for various lay-up specifications [9-10]. Della and Shu [2007] reviewed analytical models and numerical analysis for the free vibration of delaminated composites. The models were classified according to fundamental theoriesand assumptions. They presented and compared the results of some of the models. Also they have discussed the influence of delamination on the natural frequencies and mode shapes of the composite laminates. Andraset.al [2015] have studied on free vibration of laminated composite beams. They have modeled delaminated composite as simply layered beam elements. The coupling between the flexural and longitudinal vibration is considered in the delaminated part by periodic normal forces during the free vibration of the system. Mihai and Constantin [2014] studied different possible cases of the impact between the empennage and an external body with different consistencies: a rigid one and an organic tissue one (e.g. a bird). In order to correctly describe the deformation and rupture of the empennage, due to the high strain rate the Johnson–Cook material model was used in their study. Suleyman at al. [2014] studied on the nonlinear dynamic response of a hybrid laminated composite plate composed of basalt, kevlar/epoxy and glass/epoxy under the blast load and also investigated the damping effects. Tian et al. [2014]

studied the dynamic performances of high-speed train are analyzed under different wind shear environments. Matadi et al. [2015] discussed the response of composite laminates subjected to low velocity impact.

Avila et al., [2007] carried out vibration analysis of fiber glass/epoxy/nano clay nanocomposites. They have presented the natural frequency, damping factor and mode shape for the laminates with and without clay. Also it was reported that dispersion of nano clay effectively improved the damping coefficient and changed the mode shapes and natural frequencies. Deshmane et al., [2007] worked on the reinforcement of PP and PE with 4 wt. % nano-clay lead to a striking variation in impact toughness behavior under identical processing conditions. Our previous studies, Velmurugan and Balaganesan [2013] and [2014], focused on experiments and analytical model on energy absorption of nanocomposites laminates subjected to impact loading above ballistic limits. It is observed that the presence of clay enhances the energy absorbing capacity of the laminates during perforation. In our earlier study [2011] on modal analysis of pre and post impact on nanocomposite laminates, the effect on dispersion of nanoscale fillers was studied on vibration parameters natural frequency and damping factor. It was observed that dispersion of nanoclay controls delamination and hence increasesthe natural frequency of nanocompositelaminates.Thenanoscale fillers act as secondary fibers in the matrix system and due to their large surface area interaction improves for better energy transfer between filler and matrix. This enhances the damping coefficient of compaoiste laminates when subject to impact. The vibration study focuses to predict vibration parameters natural frequency and damping factors. Impact loading on the composites makes the composite to vibrate after the contact time period of the projectile. The contact period depends on the velocity of the impact. For the below ballistic impact, the point of impact subjected to plastic failure and the remaining area of the laminate subjected to elastic deformation till the period of contact and the energy is disspated by the vibration of the laminate. When the impact is above ballistic limit, the most of project energy is absorbed in various failure modes and vibration. The vibration of plates at different speeds of impact is not seen in the literature. Hence it is proposed to study the dynamic response of nanocomposites for low, medium and high velocity impact loading.

In this work, an attempt wasmade to find the response of the laminates acceleration and period of vibration for different impact loading conditions. The laminates wereprepared from WRM glass fiber/epoxy with 1-5 weight % of nano filler.The effect of nano clay incorporation in the glass/epoxy fiber laminates, with orientation of 0°/90°, wasstudied for low, medium and high velocity impact loading. The damping factors values wereobtained for the laminates subjected to low velocity impact and the effect of nano clay wasstudied.

Experiments

Preparation of Specimens

The nano composite laminates were fabricated in two steps. Clay was mixed with resin using shear mixer at 750 RPM for 2hrs and kept in the vacuum oven to remove the air bubbles at room temperature, for better dispersion. Glass fiber woven roving mat (WRM) of 610 gsm was used for this work. Hardener, TETA of 10% was mixed with the epoxy-clay mixture, by weight. The laminates were prepared by hand lay-up technique and then compressed in compression molding machine. Laminates with 3, 5 and 8 layers of WRM size 300mm x 300mm were prepared for testing.

Fig. 1(a) shows the TEM image of the nano clay dispersed with epoxy matrix. The cross section of the clay is in few nano meters and the length is in micron size. Fig. 1(b) shows the TEM image of bunch of clay layers. The clay has high aspect ratio which acts as secondary fibers when reinforced with matrix. Magnicium and Silica are the major elements in clay.
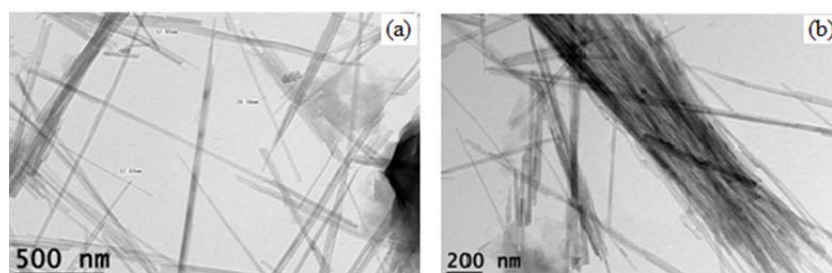

FIG. 1 TEM IMAGE OF (a) NANO CLAY (b) A BUNCH OF CLAY

Drop Mass Test

The impact test is performed using drop mass setup and the spherical nose projectiles are used for the test. The plate is fixed horizontal plane in the fixture which supports all the four sides of the laminate of size 300mm x 300mm. An accelerator is fixed in the bottom side of the plate to measure the time response. The projectile of mass 558 grams is fixed in a circular plate, and the total mass of 2.45kg is dropped from 0.25m and 0.5m heights with maximum velocities at the time of strike as 2.21 m/s and 3.13 m/s by using electro magnet. The corresponding energy released by the drop mass is 6J and 12J respectively. From the time response curve, the damping factor of the laminate for particular impact velocity is calculated using logarithmic decrement method. The formula for finding damping factor (ζ) using logarithmic decrement method is

$$\zeta = \delta^2 / (4\pi^2 + \delta^2)^{0.5} \tag{1}$$

Projectile Impact Test

In projectile impact, the impact velocities are considered below and above the ballistic limit. The projectile of diameter 9.5 mm with spherical nose of mass 7.6g is used for this study. As the velocity of impact is well within ballistic velocity, the strain in the fibers is below the failure strain and within the elastic region. This causes the rebound of the projectile as well as vibration of the laminate. A shock accelerometer of capacity 100kg, PCB make, model No. 350B21, is used to capture the response through the Data Acquisition (DAQ) Card [NI-PXI 4472] and the response is recorded in a personal computer. The accelerometer is fixed at a distance ¼ length of diagonal, from one of its corner which is also a non-nodal line. The projectile is impacted at the center of the laminates. The time response and frequency response of the laminates are obtained. The time response curve is discussed for the acceleration, time period of vibration, effect of clay presence in the matrix and thickness of the laminates. Fig. 2 (A) shows gas gun set up used for projectile impact loading. Laser diode is used to predict velocity of projectile before impact on target and residual velocity is predicted by two aluminium foil circuit method for above ballistic impact. The velocity range is obtained by changing pressure of gas in the chamber. Fig. 2 (B) shows drop mass impact testing facility for conducting low velocity impact.
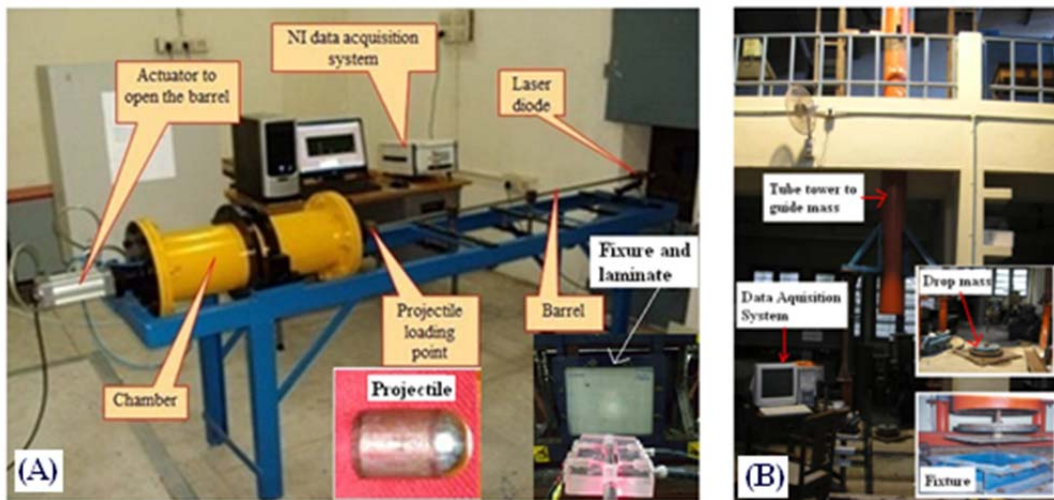

FIG. 2 (A) GAS GUN EXPERIMENTAL SET UP FOR IMPACT TESTING, (B) DROP MASS SET-UP

Results and Discussions

Impact Response during Drop Mass Test

1) Impact Response

Dropmass test were carried out in the three layer laminates with and without clay. The plate is fixed horizontal plane in the fixture which supports all the four sides of the laminate of size 300mm x 300mm. Figs. 3 and 4show time response curve for the impact velocities 2.21 m/s and 3.13 m/s for different fractions of clay additions. The vibration of laminate without clay at velocity 2.21 m/s is nullified in 500 ms, for 5% clay ocillation is nullified

within 150 ms.It is also noticed that the number of ocillations reduced for increase in velocity. For 1% clay at velocity 2.21m/s vibration is nullified only after 400 ms, at velocity 3.13 m/s the vibration is nullified after 200 ms. In the lowest velocity of impact the contact time between the specimen and the projectile is more not only due to low velocity but also the drop energy isnot sufficient to penetrate the laminate. Since the contact time is more and most of the energy is converted into vibration, but in high velocities part of the energy dissipates to penetrate the laminate and the remaining energy is used in vibration. When the velocity increases, the contact time between the specimen and projectile decreases and impact damage i.e., penetration level of projectile increases. But it is observed that for the same velocity level increase in clay addition controls the impact damage and also oscillations are very much controlled.
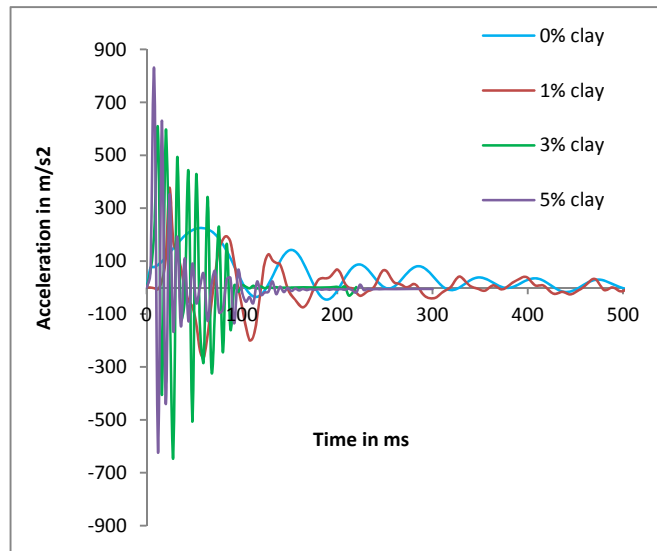

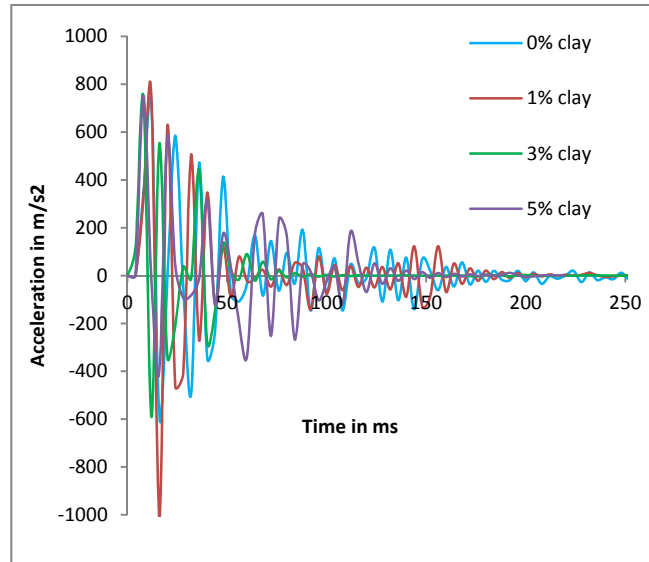FIG. 3TIME RESPONSE CURVE OF LAMINATES AT THE VELOCITY OF 2.21 M/S

FIG. 4TIME RESPONSE CURVE OF LAMINATES AT THE VELOCITY OF 3.13 M/S

2) *Damping Factor*

The damping factor values of the laminates are obtained from logarithmic decrement method. The maximum acceleration values in successive oscillations are considered to find logarithmic values and the damping factor values are obtained. Fig. 5 shows the damping factors of the laminates with and without clay subjected to impact velocities 2.21 m/s and 3.13 m/s. The damping factor for the laminate without clay is 0.031 when subjected to impact at 2.21 m/s. The damping factor for the laminate with 1% clay is 0.048 and the increase is about 56% when compared to laminate without clay. The damping factor values for the laminates with 3% and 5% clay are 2 and 2.2 times of damping factor of the laminate without clay. The damping factor for the laminate

without clay subjected to impact velocity 3.13 m/s, is 0.036. The increase in damping factor for the laminate with 1% clay is about 40% higher than the laminate without clay. The damping factor values for the laminate with 3% and 5% clay are 1.77 and 2.2 times higher than the laminate without clay. The damping factor for impact velocity 2.21 m/s is less than that at 3.13 m/s. This is due to the higher contact time between the specimen and the projectile at low velocity the vibration developed is high and also as discussed earlier, most of the energy at low velocity is converted into vibration which leads to low damping factors. But it is observed that increase in nano clay percentage appreciably controls the amplitude ofacceleration and increases the damping factor. For higher velocities the damping factor value increases due to low contact time and low vibration energy is dissipated in the laminate. Hence it is clear that addition of clay in the matrix enhances damping capacity of the composite laminates.
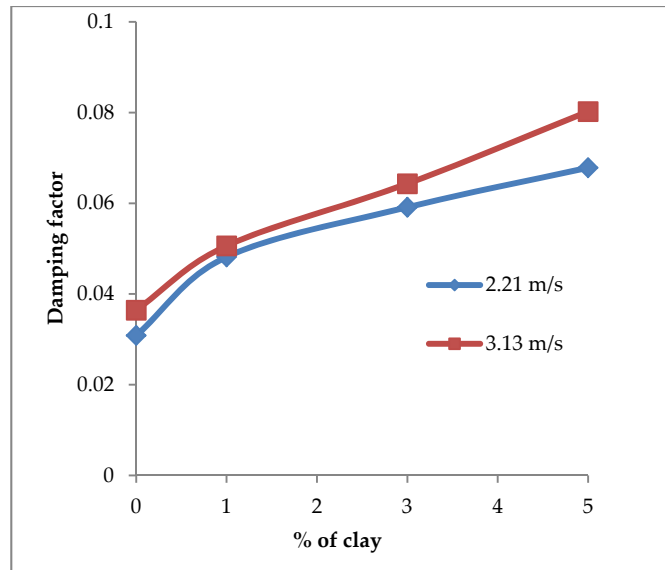

FIG. 5DAMPING FACTOR OF THE LAMINATES SUBJECTED TOIMPACT VELOCITIES 2.21 m/s AND 3.13 m/s

Time Response of the Laminates during Projectile Impact

The laminated composite plates of 3, 5 and 8 layers with and without clay are subjected to impact by projectile velocities below and above the ballistic limit. The tests are carried out to determine the time response during vibration by using a shock accelerometer. When the projectile is impacted on the laminate, the laminate vibrates and then decaysin its acceleration of vibration. Here, the acceleration values are plotted against the time. The changes in amplitude and time period for different velocities of impact, thickness of the laminate and effect of clay dispersion are discussed for various impact velocities of projectile.

1) Time Response of Three Layer Laminates

Figs. 6-9 show time response for acceleration for three layer laminates with and without clay when subjected to 35m/s, 65 m/s, 110 m/s and 135 m/s. In theses velocities, 35 m/s and 65 m/s are below the ballistic limit and 110 m/s and 135 m/s are above the ballistic limit. Fig. 6 shows time response curve for laminates without clay. The maximum acceleration value is about 57000 m/s^2 at 35 m/s and is about 5000 m/s^2 at 135 m/s. The decay of amplitude of acceleration is taken 70 ms for 35 m/s and 17 ms for 135 m/s. When the laminates are subjected to impact below ballistic limit, the laminates dissipates energy in vibration mode. Whereas this energy is less in case, the impact velocity is above the ballistic limit.

Fig. 7 shows time response curve for laminate with 1% clay. The maximum acceleration is about 78000 m/s^2 for the laminate when subjected to 65 m/s. The maximum acceleration values for 110 m/s and 135 m/s are less than 10000 m/s^2. The period is less than 20ms for these velocities.

Fig. 8 shows for the laminates with 3% clay, the maximum acceleration for this laminate is about 50000 m/s^2 at 35 m/s. The maximum acceleration is about 80000 m/s^2 for the laminate subjected to 65 m/s.

Fig. 9 shows time response curve for laminates with 5% clay. The maximum acceleration for the laminate subjected to 65 m/s is about 90000 m/s². The maximum acceleration values for 110 m/s and 135 m/s are less than 10000 m/s² which is similar to other laminates. At higher velocities of impact there are not many changes observed in maximum acceleration and time period.
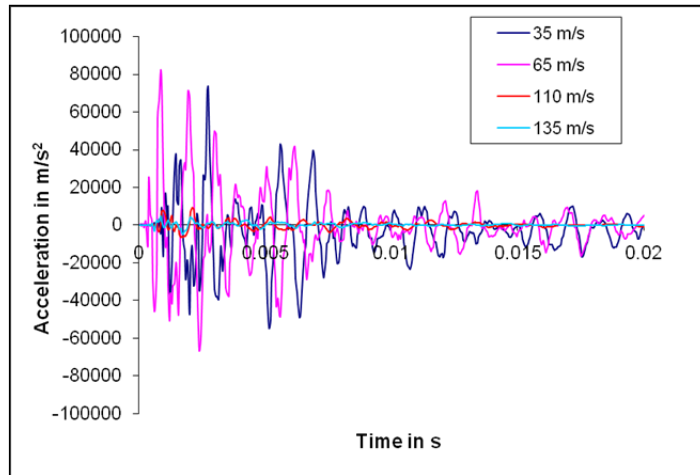

FIG. 6 ACCELERATION-TIME RESPONSE FOR THREE LAYER LAMINATE
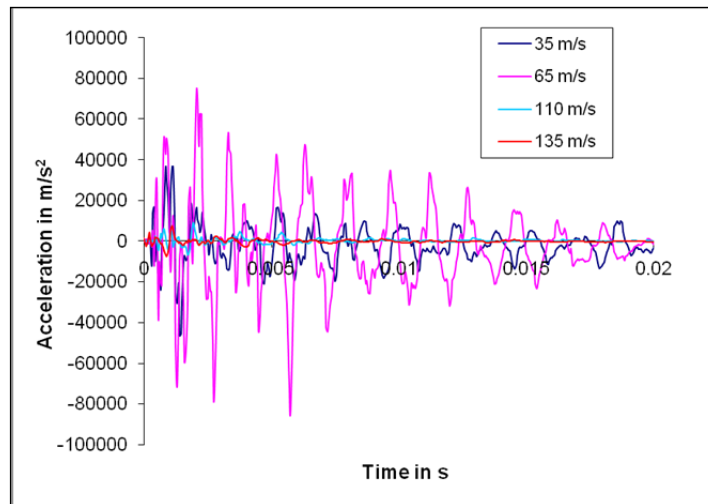WITHOUT CLAY FOR FOUR DIFFERENT VELOCITIES

FIG. 7 ACCELERATION-TIME RESPONSE FOR THREE LAYERLAMINATE
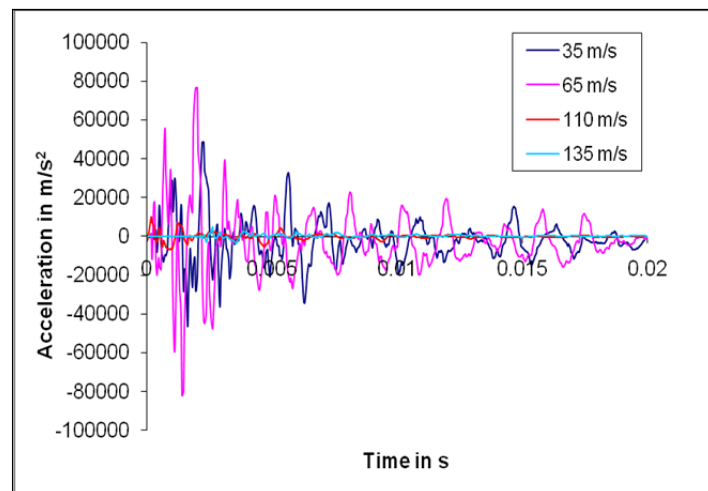WITH 1% CLAY FOR FOUR DIFFERENT VELOCITIES.

FIG. 8 ACCELERATION-TIME RESPONSE FOR THREE LAYERLAMINATE
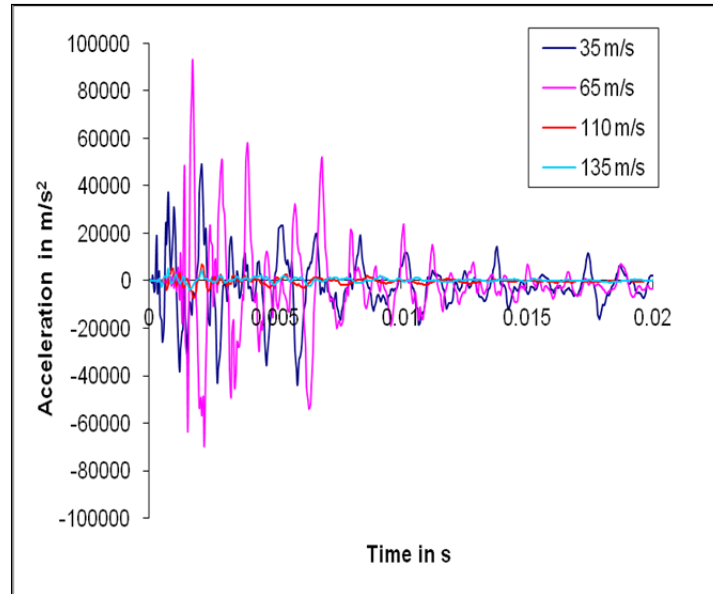WITH 3% CLAY FOR FOUR DIFFERENTVELOCITIES.

FIG. 9ACCELERATION-TIME RESPONSE FOR THREE LAYERLAMINATE
WITH 5% CLAY FOR FOUR DIFFERENT VELOCITIES.

2) *Time Response of Five Layer Laminates*

Figs. 10 shows the time response of 5 layer laminates without clay subjected to impact velocities below and above ballistic limit. The plot shows the vibration period for 20 ms. The number of oscillations in the 20 ms is about 26 whereas in the 3 layer laminate it is about 13 which is seen in Fig. 6. The maximum amplitude of acceleration for impact velocity of 65 m/s, is about 100000 m/s². The maximum acceleration values for the impact velocities 135 m/s and 152 m/s are less than 10000 m/s². Fig. 11 shows the corresponding curves for laminate with 1% clay. It is observed that the maximum acceleration is about 125000 m/s². The number of oscillations in 20 ms is same as in the laminate without clay.

Figs. 12 and 13 show time response of the laminates with 3% and 5% clay respectively. The maximum acceleration values are about 150000 m/s² and 80000 m/s² respectively for the laminates with 3% and 5% clay for the velocity of impact at 65 m/s. The decay of acceleration is nullified in 20 ms for the laminate with 5% clay. It is seen that as the clay amount in laminate is increased, the maximum amplitude of acceleration decreases where due to the increase in damping factor of the laminates with high clay content.
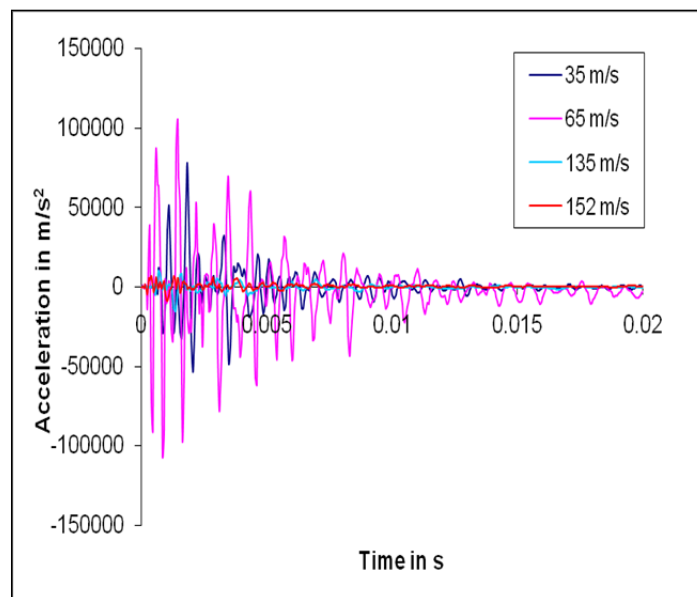

FIG. 10ACCELERATION-TIME RESPONSE FOR FIVE LAYERLAMINATE
WITHOUT CLAY FOR FOUR DIFFERENTVELOCITIES
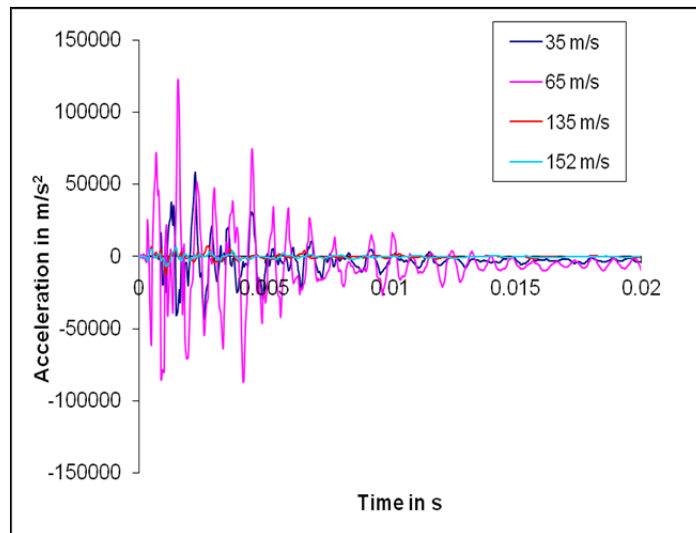
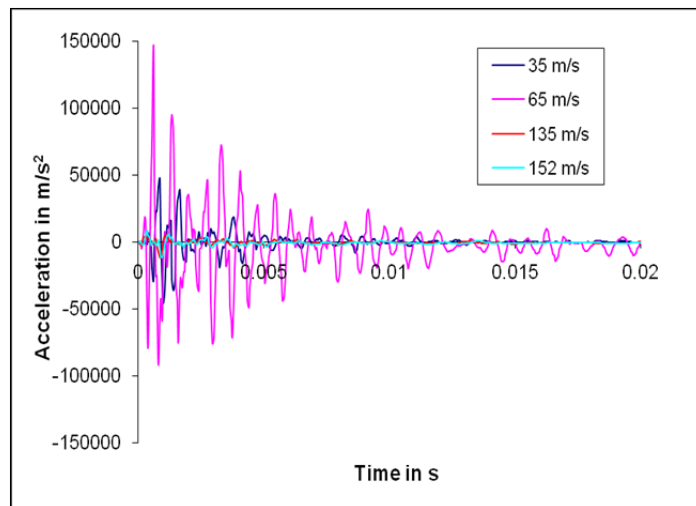FIG. 11ACCELERATION-TIME RESPONSE FOR FIVE LAYER LAMINATE WITH 1% CLAY FOR FOUR DIFFERENT VELOCITY

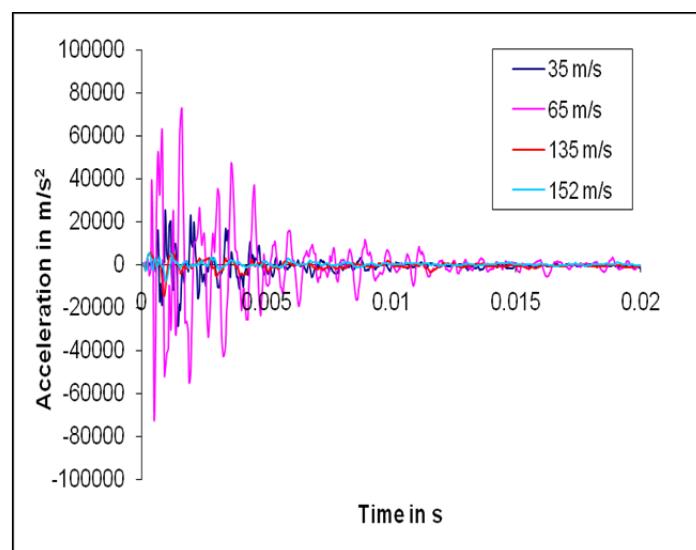FIG. 12ACCELERATION-TIME RESPONSE FOR FIVE LAYER LAMINATE WITH 3% CLAY FOR FOUR DIFFERENT VELOCITIES

FIG. 13ACCELERATION-TIME RESPONSE FOR FIVE LAYER LAMINATE WITH 5% CLAY FOR FOUR DIFFERENT VELOCITIES

3) Time Response of Eight Layer Laminates

Figs. 14–17 show the time response of 8 layer laminates with and without clay subjected to impact velocities below and above ballistic limit. The plot shows the vibration period for 20 ms. The number of oscillations in the 20 ms is more than 50 which is high compared to 3 and 5 layer laminates. The maximum acceleration is observed for impact velocity of 65 m/s, the value is about 80000 m/s^2. The maximum acceleration value for the impact velocities 135 m/s and 152 m/s are similar to 3 and 5 layer laminates. The complete decay in acceleration of vibration is observed in 20 ms.This is because of the increase in thickness of the laminates. As the thickness of the laminate increases, the stiffness of the laminates also increases which results in increased number of oscillations.

Fig. 15 shows the time response for the laminate with 1% clay. It is observed that the maximum acceleration is about 80000 m/s^2 for 35 m/s and 65 m/s velocities of impact. The maximum acceleration value at 204 m/s is half of the maximum acceleration value at 152 m/s.

FIG. 14 ACCELERATION-TIME RESPONSE FOR EIGHT LAYER LAMINATE
WITHOUT CLAY FOR FOUR DIFFERENT VELOCITIES

FIG. 15ACCELERATION-TIME RESPONSE FOR EIGHT LAYER LAMINATE
WITH 1% CLAY FOR FOUR DIFFERENT VELOCITIES

Figs. 16 and 17 show acceleration-time response of laminates with 3% and 5% clay respectively. The maximum acceleration values are about 100000 m/s^2 for laminates with 3% and 5% clay for the velocity of impact 65 m/s.

The decay of acceleration signal is nullified in 20 ms similar to other 8 layer laminates. In 8 layer laminates, there arenotmany changes in the maximum acceleration values for below ballistic limit. For velocities above ballistic limit, the maximum acceleration values for 204 m/s are less than the maximum acceleration values at 152 m/s.
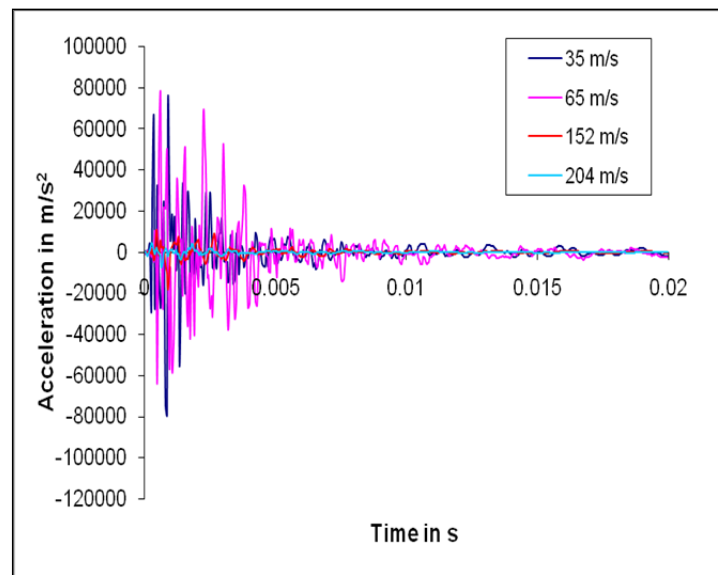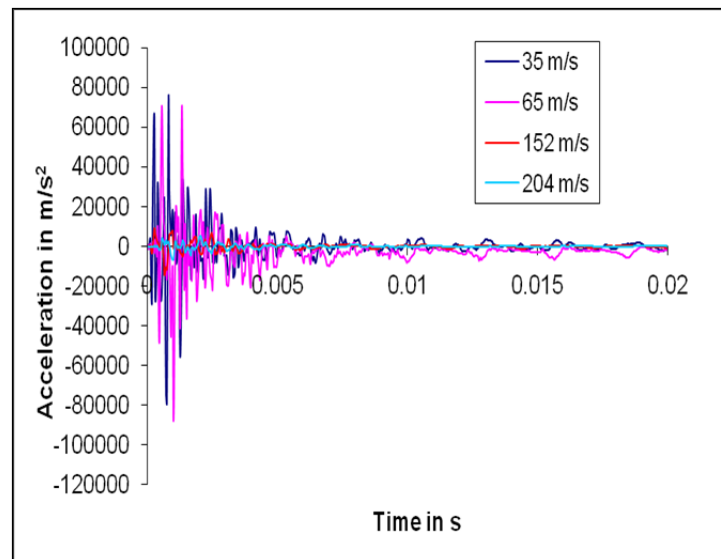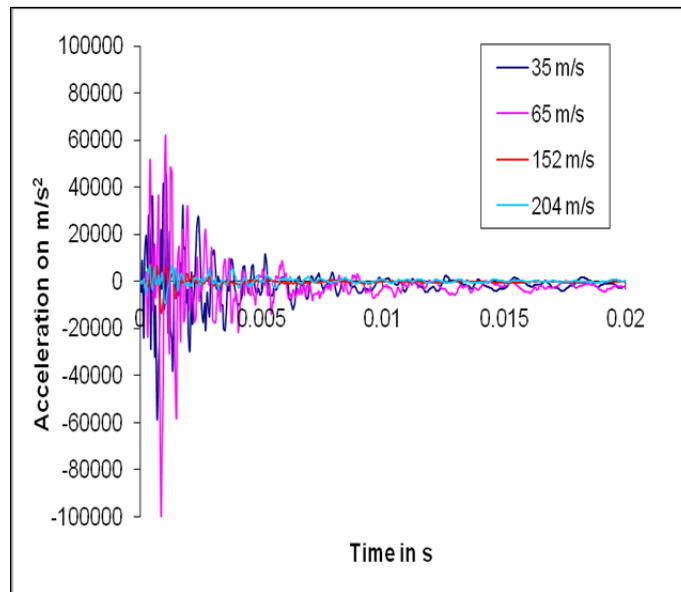

FIG. 16ACCELERATION-TIME RESPONSE FOR EIGHT LAYER LAMINATE
WITH 3% CLAY FOR FOUR DIFFERENT VELOCITIES
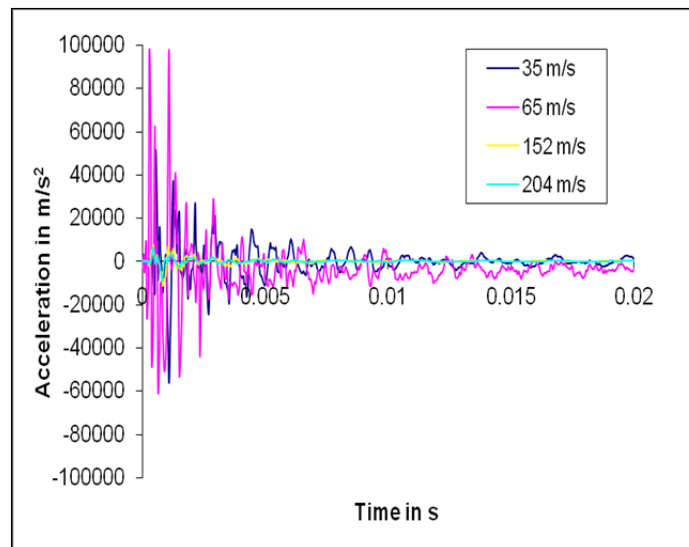
FIG. 17 ACCELERATION-TIME RESPONSE FOR EIGHT LAYER LAMINATES
WITH 5% CLAY FOR FOUR DIFFERENT VELOCITIES

Effect of Clay Dispersion in Response

The results for the maximum acceleration and the corresponding period of time are shown in Table 1 for three layered laminates of velocity 35 m/s and 135 m/s respectively. At 35 m/s, the maximum acceleration values of laminates with clay are less than the laminates without clay. The maximum acceleration values are decreasing up to 3% clay and increasing up to 5% clay. The period of time for vibration is 70 ms for laminate without clay and it is decreasing up to 3% clay then remains almost the same. At 135 m/s, the maximum acceleration values are less than 10% of the values at 35 m/s. The maximum acceleration values are decreasing up to 3% clay and increasing for 4% and 5% clay. The time period for vibration is less than 20 ms in all the cases. As the impact velocity increases, the time period of oscillations decreases. This is because at high velocities the vibrational energy is less than the energy absorbed in other modes.

TABLE 1 ACCELERATION AND TIME TAKEN FOR VIBRATION DURING IMPACT
FOR 3 LAYER LAMINATE WITHOUT CLAY AT 35 M/S AND 135 M/S

Laminate	Velocity-35 m/s		Velocity-135 m/s	
	Maximum acceleration in m/s²	Time in ms	Maximum acceleration in m/s²	Time in ms
Without clay	75325	70	5072	17
1% clay	56522	68	4919	17
2% clay	53436	67	4965	16
3% clay	48522	66	4893	16
4% clay	49127	66	5859	15
5% clay	52928	66	6680	16

Table 2 shows the maximum acceleration and time period for 5 layer laminate at 35 m/s and 152 m/s velocities of impact. The maximum acceleration value of laminate without clay at 35 m/s is 75265 m/s², and the value is decreasing up to 5% clay. The time period for vibration is between 26 ms and 35 ms. At 152 m/s, the maximum acceleration values are decreasing for laminates with 5% clay and the time period is between 10 ms and 15 ms.The maximum acceleration in laminates without clay is higher than that in laminates with clay. This shows that the clay layers act as a cushion and absorbs the energy. In other words, it is due to the increase in damping factor of the laminates with clay.

TABLE 2ACCELERATION AND TIME TAKEN FOR VIBRATION DURING IMPACT FOR 5 LAYER LAMINATE WITHOUT CLAY

AT 35 M/S AND 152 M/S Laminate	Velocity-35 m/s		Velocity-152 m/s	
	Maximum acceleration in m/s²	Time in ms	Maximum acceleration in m/s²	Time in ms
Without clay	75265	35	6872	15
1% clay	55545	32	6286	13
2% clay	51170	30	5694	13
3% clay	50697	30	5590	12
4% clay	45447	29	5548	10
5% clay	35613	26	5515	10

Table 3 shows the maximum acceleration and time period for 8 layer laminates at 35 m/s and 204 m/s velocities of impact. The maximum acceleration value of laminate without clay at 35 m/s is high, and the value is decreasing up to 5% clay. The time period for vibration is between 23 ms and 27 ms. For 204 m/s, the maximum acceleration values are decreasing for laminates with clay up to 5%. Also it is observed that the time period decreases from 10 ms to 8 ms as the clay percentage increases.

Fig. 18 shows the microscopic images of fractured surface of three layer laminates subjected to velocity of 85 m/s. Fig. 18(a) shows the fractured surface of laminate without clay. It shows failure of fibers for about 8 mm width in the impacted zone of the laminate and the velocity of impact is below the ballistic velocity of the laminate. It clearly shows that the energy possessed by projectile is absorbed by the failure of matrix and fiber. Fig. 18(b) shows the fracture surface of laminate with 1% clay subjected to the velocity of 85 m/s. It is observed that the failure zone of fibers is about 3 mm in width and failure of matrix is noticed in the impacted zone. In Fig. 18(c), for laminate with 2% clay, the failure zone of fiber is noticed for about 2 mm width and complete crack of matrix is seen in the impacted and surrounding zone. For laminates with 3% clay, subjected to the same impact velocity, there is no complete failure of fiber noticed in the point of impact, but there is partial crack in a strand. But the failure of matrix of about 8 mm width is seen in the impacted zone, which is shown in Fig. 18(d). Fig. 18(e) shows the failure of impacted zone of laminate with 4% clay. The failure of fiber is completely absent and the crack in the matrix is noticed in concentric form around the point of impact. This is due to the propagation of stress waves towards the boundary from the impact point. Due to the impact, partial separation of matrix is noticed. When the laminate with 5% clay is subjected to impact, after the failure of matrix the fiber is partially failed within the range of about 3 mm in both

warp and weft directions. This is shown in Fig. 18(f). Clay dispersion in matrix improves energy absorption due to impact loading and it protects failure of fiber. For 1% and 2% clay dispersion in matrix, partial failure of fiber and matrix is observed. For laminate with 3% and 4% clay, most of the impact energy is absorbed by the matrix and the fibers are protected. But for 5% clay dispersion, crack is observed in the matrix due to brittleness of matrix.

TABLE 3 ACCELERATION AND TIME TAKEN FOR VIBRATION DURING IMPACT
FOR 8 LAYER LAMINATE WITHOUT CLAY AT 35 M/S AND 204 M/S

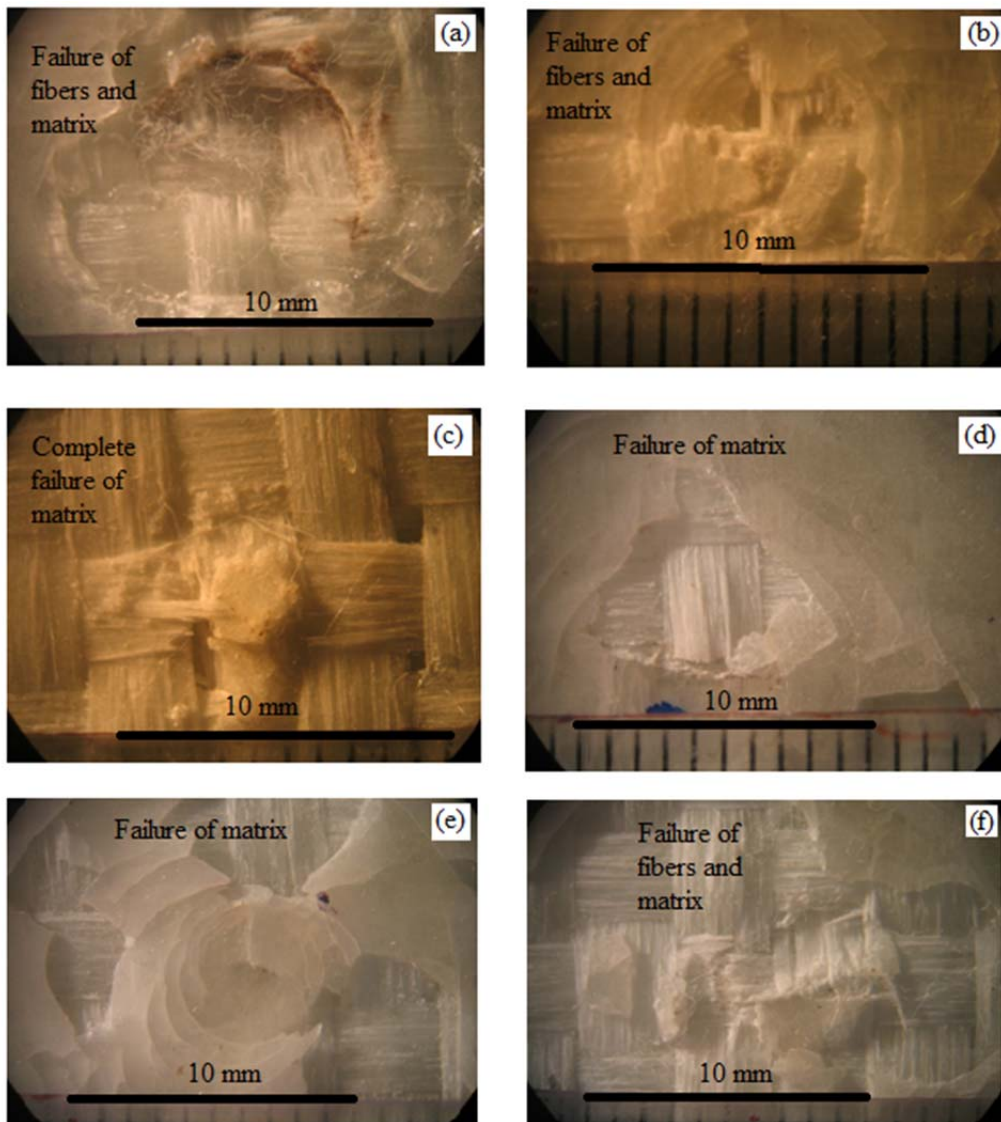| Laminate	Velocity-35 m/s		Velocity-204 m/s	
	Maximum acceleration in m/s²	Time in ms	Maximum acceleration in m/s²	Time in ms
Without clay	82651	27	6433	10
1% clay	80538	27	6146	10
2% clay	57753	26	5841	9
3% clay	62392	26	5872	9
4% clay	51481	24	5677	8
5% clay	50593	23	5411	8

FIG. 18FRACTURED SURFACE OF THREE LAYER LAMINATES SUBJECTED TO IMPACT VELOCITY OF 85 M/S (A) WITHOUT CLAY (B) WITH 1% CLAY (C) WITH 2% CLAY (D) WITH 3% CLAY (E) WITH 4% CLAY (F) WITH 5% CLAY, VELMURUGAN AND BALAGANESAN [2013].

Conclusions

Composite laminates of three, five and eight layers are subjected to impact by drop mass for low velocity impact and projectile impact at velocities below and above the ballistic limit with clamped in all the edges. The shock accelerometer recorded the acceleration response of the laminates during impact of the projectile.

- Nano clay dispersion in matrix enhances damping factor in low velocity impact and reduces the period of vibration.

- In projectile impact, the maximum amplitude of acceleration values for velocities below ballistic limit is higher than that for velocities above ballistic limit.

- The maximum amplitude of acceleration values for the laminates subjected above ballistic limit are less than 10% of maximum amplitude of acceleration values of laminates of velocities below ballistic limit. The maximum amplitude of acceleration values are increasing up to a threshold velocity below ballistic velocity and decreases further in increase of velocity.

- The time period for vibration below ballistic limit is higher than that for velocities above ballistic limit.

- The number of oscillations for three layer laminates are less than five and eight layer laminates in a time period of 20 ms. Number of oscillations increases as the thickness of the laminate increases.

REFERENCES

[1] AndrasSzekrenyes, A special case of parametrically excited systems: Free vibration of delaminated composite beams, Eupoian Journal of Mechanics A/Solids, 49(2015), 82-105.

[2] Avila, A., M.I. Soares and A.S. Neto (2007) A study on nano structured laminated plates behavior under low-velocity impact loadings. *International journal of impact engineering*, 24, 28-41.

[3] Balaganesan G, R. Velmurugan, M. Srinivasan, N. K. Gupta and K. Kanny Energy absorption and ballistic limit of nanocomposite laminates subjected to impact loading, International Journal of Impact Engineering 2014; 74: 57-66.

[4] Borvik T, Hopperstad OS, Langseth M, Malo KA. Effect of target thickness in blunt projectile penetration of Weldox 460 E steel plates. IntJImpEng 2003; 28: 413-464.

[5] Della, C.N. and D. Shu (2007) Vibration of Delaminated Composite Laminates: A Review. *Applied Mechanics Reviews*, 60, 1-20.

[6] Deshmane, C., Q. Yuan, R.S. Perkins and R. D. K. Misra (2007) On striking variation in impact toughness of polyethylene–clay and polypropylene–clay nanocomposite systems: the effect of clay–polymer interaction. *Material Science Engineering A*, 458(1–2), 150–157.

[7] Garcia-Castillo SK, Sanchez-Saez S, Lopez-Puente J, Barbero E, Navarro C. Impact behaviour of preloaded glass/polyester woven plates. Compos SciTechnol 2009; 69:711-717.

[8] Lee DG, Lim TS, Cheon SS. Impact energy absorption characteristics of composite structures. *Compos Struct* 2000; 50: 381-390.

[9] Leissa, A.W, *Vibration of plates*. Scientific and Technical Information Division of NASA, NASA SP-160, Washington, 1969.

[10] Mahi, A.E.I., M. Assarar *Journal of Adhesion Science Technology*,

[11] Y. Sefrani and J.M. Berthelot (2008) Damping Analysis of orthotropic composite materials and laminates. *Composites: Part B*, 39, 1069-1076

[12] Miyagaw .H and L.T. Drzal (2004) The effect of chemical modification on the fracture toughness of montmorillonite clay/epoxy nanocomposites., 18(13), 1571–1588.

[13] Nieves, F.J., F. Gascon and A. Bayon (2004) Natural frequencies and mode shapes of flexural vibration of plates: laser-interferometry detection and solutions by Ritz's method. *Journal of Sound and Vibration*, 278, 637–655.

[14] Ohta, Y., Y. Narita and K. Nagasaki (2002) On the damping analysis of FRP laminated composite plates. *Composite Structure*, 57,169–175.

[15] Osman, M.A. and A. Atallah (2005) Interparticle and particle–matrix interactions in polyethylene reinforcement and visco elasticity. *Polymer,* 46(22), 9476–9488.

[16] R. MatadiBoumbimba, C. Froustey , P. Viot, P. Gerard, Low velocity impact response and damage of laminate composite glass fibre/epoxy based tri-block copolymer, *Composites Part B*, 76(2015), 332-342

[17] Roland, L. Woodcock, R.B. Bhat and I.G. (2008) Stiharu Effect of ply orientation on the in-plane vibration of single –layer composite plates. *Journal of sound and vibrations*, 312, 94-108.

[18] SüleymanBaştür, k HaydarUyanık, ZaferKazanc. Nonlinear damped vibrations of a hybrid laminated composite plate subjected to blast load, Procedia Engineering, 88(2014), 18-25.

[19] Sun L, Ronald F. Gibson, Gordaninejad F, Suhr J. Energy absorption capability of nano composites: A review. Compos SciTechnol 2009; 69: 2392-2409.

[20] Velmurugan R, Balaganesan G. Energy absorption capability of glass/epoxy nano composite laminates. Int J Crash 2013; 18: 82-92.

[21] Velmurugan. R and Balaganesan. G (2011) Modal analysis of pre and post impacted nano composite laminate, Latin American Journal of Solids and Structures, 8, 9-26.

[22] Viana, J. C (2006) Polymeric materials for impact and energy dissipation. Plast Rubber. *Composites*, 35(6–7), 260–267.

[23] Mihai Ivanica, Constantin Rotaru. Numerical Investigation of an Impact Between an External Body and an Aerodynamic Surface. *Frontiers in Aerospace Engineering*, 2014, 3(2), 56-63. doi: 10.14355/fae.2014.0302.04

[24] Tian Li, Jiye Zhang, Yisheng Zou, Weihua Zhang. Dynamic Performances of High-speed Train in Wind Shear. *Frontiers in Aerospace Engineering*, 2014, 3(1), 17-22. doi: 10.14355/fae.2014.0301.03.

G. Balaganesan Chennai, Tamilnadu, India. 02.09.1970

Ph. D in Aerospace Engineering, Indian Institute of Technology Madras, Chennai – 600036, Tamilnadu, India. His research area is impact studies on composites and repair of pipes and composites.

He is in-charge of the institute students training facilities that has as many as power tools for wood working, metal working, foundry, smithy, welding, composites, plastics, modern machine shops and laboratories of basic electrical, electronics, pneumatics and hydraulics for imparting hands-on training to the students, He has been involved in teaching-learning in this environment for the past 15 years or so with a constant interaction with the students.

Fire-II Flight Data Simulations with Different Physical-Chemical Kinetics and Radiation Models

S. Surzhikov[1] and J. Shang[2]

Institute for Problems in Mechanics Russian Academy of Sciences (IPMech RAS)[1], Center for Basic and Applied Research, All-Russian Research Institute of Automatics, Moscow, 119526, Russia

And Wright State University[2], Dayton, OH 45435

Abstract

Two chemical kinetics models by Park, Dunn and Kang are implemented with the options of gasdynamic-radiation coupling and two nonequilibrium dissociation assumptions. A series of systematic simulations have been successfully conducted in examining these effects on the total heat transfer rates, standoff distance, and temperature profiles along the stagnation streamline. For the first time, an *ab-initio* quasi-classic and quantum mechanical approach is used to generate the optical properties including the radiative properties at the spectral level for atoms and ions. An increased radiative heat transfer rate of more than a factor of two is realized at trajectory points $1634 < t < 1643$s through the new atomic lines spectral property to the two well-known chemical kinetics models.

Keywords

Hypersonic, Reentry, Radiation

Nomenclature

$c_{p,i}$	Specific heat capacity at constant pressure, J/(mol·K)
c_p	Specific heat capacity for translational and vibrational degree of freedom, J/(mol·K)
D_i	Effective diffusion coefficient of species, m²/
$\dot{e}_{V,m}$	Rate of the volumetric vibration energy generation in *m-th* mode, J/cm³·s
h_i	Specific enthalpy, J/mol
$J_{b,\omega}(\mathbf{r})$	Black body spectral intensity (the Planck function), J/(s·cm⁻¹·cm²·sr)
$\mathbf{J}_i$	Mass diffusion flux, $\mathbf{J}_i = -\rho D_i \,\mathrm{grad}\, Y_i$, kg/(m²·s)
$J_\omega(\mathbf{r}, \mathbf{\Omega})$	Spectral intensity of heat radiation, J/(s·cm⁻¹·cm²·sr)
$Q_\omega(\mathbf{r})$	Spectral emission source, J/(s·cm⁻¹·cm³·sr)
$\kappa_\omega(\mathbf{r})$	Spectral absorption coefficient, cm⁻¹
M^+, M^-	Half-moment characteristics, W/cm²
N_s	Number of gas species
N_V	Number of vibrational modes
Q_{vib}	Energy source due to vibrational relaxation, J/(s·cm³)
p	Pressure, J/m³
t	Time, s
T	Translational temperature, K
$\vec{\vec{\tau}}$	Viscous stress tensor
$\dot{w}_i$	Reaction rate for species, kg/(cm³·s)

---

1 Professor, Deputy Director, Head of the Radiative Gasdynamic Laboratory, AIAA Fellow.
2 Research Professor, Wright State University, AIAA Fellow.

$\mathbf{V}(u,v)$	Velocity, m/s
Y_i	Mass fraction of species i
λ	Heat conductivity coefficient, J/(m·K)
μ	Viscosity coefficients, kg/(m·s)
ρ_i	Density and mass diffusion flux for species, kg/m³
Φ_μ	Dissipative function, J/(s·m³)
$\mathbf{\Omega}$	Unit vector of solid angle
ω_{min}, ω_{max}	Minimal and maximal wavenumber of the full spectral region of heat radiation, cm⁻¹

Introduction

The flight data of the Fire-II experimental program have been used for validation of physical-chemical models and computer codes for the aerophysics of reentry vehicles for more than 40 years [1-3]. Nevertheless, it is well known that several basic issues of aerophysics for the reentry probe simulation still remain. These are: the development of kinetic models for non-equilibrium dissociation, ionization, relaxation and radiation processes, the development of efficient CFD tools for solving the governing equations on both structured and unstructured two- and three dimensional grids, and the need for adequate models for turbulent flow and laminar-turbulent transition. For example, it was shown recently that the chemical kinetic models for the nonequilibrium Fire-II simulation leads to different predicted temperatures by a wide range, 3000 to 5000 K within the shock layer [4,5]. Such disparities were also shown in a book by Park in the early 1990's [6]. Several recent publications also demonstrate significant influence of chemical and physical kinetics on radiative heating of a new generation of space vehicles [7-10].

The uncertainty in numerical predictions of convective and radiative heating of the reentering capsule using different models of chemical and physical kinetics will be analyzed by the present study. These calculations are performed with models of chemical kinetics of Dunn and Kung [11] and Park [12]. Two different models of dissociation are used; the first one takes into account differences between translational and vibrational temperatures for N_2, O_2 and NO in the frame work of the Treanor-Marrone model [13], and the second one is the one-temperature model assuming local thermal equilibrium (LTE). All calculations are repeated to investigate the influence of atomic lines and the coupling between radiation and gasdynamics. Spectral optical properties of high temperature air are calculated by the *ab-initio*, quasi-classical and quantum mechanics approach. Each trajectory point is analyzed by several of these calculations. Additional investigations are also performed for a grid refinement study and different grid topologies.

A distinctive feature of the present effort includes the contributions by atomic and ion spectral lines to various models of physical and chemical kinetics for radiation heat transfer to a super-orbital reentry vehicle. The adopted numerical procedure for radiation transfer in the shock layer over the front shield of the space vehicle is based on the half-moment method for solving the radiation heat transfer equation with a line-by-line spectral evaluation. By this approach, the spectral optical property computations adopt the *ab-initio* technique, including parameters of atomic line strengths and half-widths.

The line-by-line spectral data calculation is carried out through a special procedure by creating an inhomogeneous distribution of optical properties with respect to wavenumber. As a consequence, it allows a significantly reduced number of the required line-by-line spectral data. It has been shown that the new line-by-line approach can achieve high accuracy with less than 80,000 nodes of data.

All numerical simulations are compared with the Fire-II flight data and have been performed by the computer programs 2D-NERAT [7-9] and ASTEROID [14,15]. This combined procedure solves the full system of interdisciplinary radiative gasdynamic equations for thermodynamically and chemically nonequilibrium gas flow which consists of the mass-averaged Navier-stokes equations, law of mass action with physical-chemical kinetic models, kinetic formulation of transport properties, and the radiation heat transfer equations in 2D/axisymmetric geometries. All computational results are compared with experimental and computational results in the open literature. The systematic simulations of radiative gas dynamics for Fire-II reentry vehicle are depicted in the form of an atlas of calculated results. The simulation at a trajectory point includes the following results: the velocity

components of the axisymmetric flowfield, pressure, density, translational and vibrational temperatures, as well as mass fractions along the stagnation streamline. Finally, the one-sided integral radiation heat fluxes, spectral distributions of radiation heat flux density, and the cumulative function are presented and delineated.

All data for Fire-II reentry vehicles are included in the present study. The computations are generated on multi-block curvilinear grids. Some detailed descriptions of the physical-chemical models and computer codes have been presented in earlier efforts [7-9]. The objective of the present study is to achieve a better understanding of the influences of different models of chemical kinetics and non-equilibrium dissociations to radiative heating on an entry space vehicle simulation. However, the impact of nonequilibrium radiative heat exchange, including the spectral lines of atoms and ions for optical property computation, is the most important objective for the current effort.

Governing Equations

The five groups of governing equations have been integrated successively into this interdisciplinary computational capability [7]. The first group of equations consists of the Navier-Stokes equations (continuity and momentum). The chemical species conservation equations of mass action constitute the second group of equations. The conservation of energy equation in non-conservative form represents the third group of equations. Equations for internal vibrational energy conservation are the forth group of equations. The system of multi-group radiation heat transfer equations composes the fifth group, and closes the system of governing equations. The first group of equations consists of the Navier-Stokes equations for global mass and momentum conservation.

$$\frac{\partial \rho}{\partial t} + \mathrm{div}(\rho \mathbf{V}) = 0, \tag{1}$$

and

$$\frac{\partial \rho \mathbf{V}}{\partial t} + \mathrm{div}\left(\rho \mathbf{V}\mathbf{V} + p\vec{\vec{I}} - \vec{\vec{\tau}}\right) = 0. \tag{2}$$

The species continuity equations, second group of equations, are formulated as:

$$\frac{\partial \rho_i}{\partial t} + \mathrm{div}(\rho_i \mathbf{V}) = -\mathrm{div}\,\mathbf{J}_i + \dot{w}_i, \quad i = 1, 2, \ldots, N_s. \tag{3}$$

The third group of equations, energy conservation equation is solved in the chain-rule-conservative form to determine directly the translational temperature. Meanwhile, it is an explicit assumption that the rotational and translational degrees of freedom of the gas mixture are equilibrated:

$$\rho c_p \frac{\partial T}{\partial t} + \rho c_p \mathbf{V} \nabla T = \mathrm{div}\left(\lambda \nabla T\right) + \frac{\partial p}{\partial t} + \mathbf{V}\nabla p + \Phi_\mu + Q_{vib} - \mathrm{div}(\mathbf{q}_R) - \sum_{i=1}^{N_s} h_i \dot{w}_i + \sum_{i=1}^{N_s} \rho c_{p,i} D_i \left(\nabla Y_i \cdot \nabla T\right), \tag{4}$$

In the above equation Φ_μ is the dissipation function, given as $\Phi_\mu = div(\vec{\vec{\tau}} \cdot \mathbf{V}) - div(\vec{\vec{\tau}}) \cdot \mathbf{V}$.

The fourth group of equations is the vibrational energy conservation equations which are formulated as:

$$\frac{\partial \rho e_{v,m}}{\partial t} + \mathrm{div}\left(\rho \mathbf{V} e_{v,m}\right) = \dot{e}_{v,m}, \quad m = 1, 2, \ldots, n_v. \tag{5}$$

The indices for the vibrational energy equation denote different species, in different energy states: m=1, 2, and 3 denote N_2, O_2, and NO of vibrational modes.

The fifth group of equations, the radiative heat transfer equation, is considered for the non-scattering gas as

$$\mathbf{\Omega} \frac{\partial J_\omega(\mathbf{r}, \mathbf{\Omega})}{\partial \mathbf{r}} + \kappa_\omega(\mathbf{r}) J_\omega(\mathbf{r}, \mathbf{\Omega}) = Q_\omega(\mathbf{r}), \tag{6}$$

where $J_\omega(\mathbf{r}, \mathbf{\Omega})$ denotes the spectral intensity of heat radiation, $k_\omega(\mathbf{r})$ is the spectral absorption coefficient and $Q_\omega(\mathbf{r})$ is the spectral emission source. At the local thermodynamic equilibrium condition $Q_\omega(\mathbf{r}) = \kappa_\omega(\mathbf{r}) J_{b,\omega}(\mathbf{r})$.

The total radiative energy flux on a surface point s with coordinate $\mathbf{r}$ and normal unit vector $\mathbf{n}$ is obtained by integrating the radiative spectral intensity, over the entire spectrum $\omega_{min} = 1000 \text{ cm}^{-1}$ to $to \; \omega_{max} = 150000 \text{ cm}^{-1}$, in a half spherical domain above the surface point,

$$W_{w,n}(\mathbf{r}) = \int\limits_{\Delta\omega_{tot}} \int\limits_{2\pi} J_\omega(\mathbf{r},\mathbf{\Omega})(\mathbf{\Omega}\cdot\mathbf{n})d\Omega d\omega = \int\limits_{\Delta\omega_{tot}} W_{w,n,\omega}(\mathbf{r})d\omega. \tag{7}$$

The coupling between radiative heat transfer and gasdynamics is achieved by sharing the pertain dependent variables of the interdisciplinary coupled system of equations. The Navier-Stokes equations are loosely coupled with the system of energy conservation equations for the translational temperature, the energy of internal degrees of freedom, and the chemical species, as well as the radiative heat transfer equation. In essence, the solutions to the axisymmetric gasdynamics conservation laws are first solved independently of the radiation equation to provide the instantaneous thermodynamic state and concentration of all chemical species which are needed in the radiative spectral coefficient calculation. Then, the radiation heat transfer equation is solved via the half-moment method in the high-temperature shock layer by the non- homogeneous plane layer formulation [16].

The method of half-moments is used for determining the integrated radiating characteristics of a flat non-uniform layer over the front surface of the Fire II probe. Equation (6) can be approximated by the equivalent system of differential equations with the spectral half-moment characteristics $M_{n,\omega}^{\pm}$:

$$\begin{aligned}\frac{dM_{n+1,\omega}^+}{d\tau_\omega} &= -M_{n,\omega}^+ + \frac{2\pi}{n+1}Q_{\omega,r} \\[2mm] \frac{dM_{n+1,\omega}^-}{d\tau_\omega} &= -M_{n,\omega}^- + \frac{2\pi(-1)^n}{n+1}Q_{\omega,r}\end{aligned} \qquad n = 1,2, \tag{8}$$

where $\varpi = \cos\theta, \quad M_{n,\omega}^+ = 2\pi\int\limits_0^1 J_\omega^+\varpi^n d\varpi, \; M_{n,\omega}^- = 2\pi(-1)^n\int\limits_0^1 J_\omega^-\varpi^n d\varpi,$ and

$$J_\omega = \begin{cases} J_\omega^+, \; 0 \le \theta \le \pi/2 \\ J_\omega^-, \; \pi/2 \le \theta \le \pi \end{cases} \tag{9}$$

For the above formulation, θ is the angle between the direction of the radiation and the outward normal of the front surface of the Fire II probe.

The transport properties of the chemically reacting gas medium are formulated by the classic kinetic theory of gases. The critical properties of the thermodynamics, chemical kinetics, and transport phenomena are provided for by electronic databases [17-21], as well as some approximate approaches [22,23]. Computer generated procedures and results have been used to obtain the spectral optical properties of all chemical compositions through the *ab-initio* approach for an accurate description of the radiative processes of gases and plasmas at nonequilibrium conditions [14,15,24-27].

The models of excitation / de-excitation of atomic species by collisional mechanisms induced by the electrons of heavy neutral species and radiative decay are well known and have been demonstrated to have acceptable accuracy for radiative heating in the aforementioned and other recently published papers. However, this approach has some significant drawbacks which have to overcome their increase reliability for aerophysics predictions. These are the imperfections of our knowledge in the elementary collision and radiative processes (which have to be included into the collisional-radiative models especially at the consideration of non-equilibrium processes) and the deficiency of our knowledge in quantum probabilities of these processes and finally, the complexity incurred in practical implementation of these models in the 2D and 3D radiative gasdynamic simulations.

We suggest one more approximate model in the present effort to be verified in regards to the problem of non-equilibrium radiation of strong shock waves in air and CO_2-N_2 (see reference 28). The general idea of the model is as follows: we adopt the vibrational mode to describe the non-equilibrium effects of dissociation and chemical kinetics, and assume that the electronic temperature approximately follows the vibrational temperature of N_2 molecules, and the electronically excited states are considered to be in equilibrium with the electronic temperature.

These assumptions were first verified in predicting non-equilibrium radiation associated with strong shock waves with an acceptable accuracy. The same assumptions are adopted in our 2D calculations.

Spectral Optical Properties and Line-By-Line Calculations

The spectral optical properties of a multi-component gas medium in the shock layer are predicted by the computer code ASTEROID [14,15]. This computer program is based on series coupled quasi-classical and quantum-mechanical models, and uses fundamental spectroscopy information, therefore all spectral optical properties are calculated by the *ab-initio* approach. It is well known that spectral lines of atoms and ions contribute significantly to radiative heat fluxes in high-temperature gases. In the following section, it will be demonstrated that the atomic line structure in the shock layer medium is extremely significant for radiation at the flight conditions of the Fire-II.

The prediction of spectral properties and calculation of radiative heat transfer with these atomic transitions are one of the pacing problems for modern aerophysics. All well-known databases were mostly created for solving astrophysics problems and spectral diagnostics of plasma. Thus the problem is that there are no available databases for radiative heat transfer and radiation gas dynamics. Atomic lines included in these specialized databases have shown a high degree of reliability. As a rule, these data are developed either by experimental means or by computational means using the most precise quantum-mechanical models. However, a common imperfection of such databases is the absence of a full set of atomic lines, omitting a large number of atomic spectral lines that have relatively low intensity.

The problems in radiation gas dynamics and radiative heat transfer for high-temperature gases and plasmas in aerospace applications put a different requirement on the databases. In this regard, it is critically important to take into account the complete spectrum of the atomic lines, because a large number of weak atomic lines can still give an appreciable contribution to radiative energy transfer.

A computational procedure by Bates and Damgaard [25] and Hartree [26] produces all the parameters needed to generate all atomic lines for atoms and ions that meet the practical interest of aerospace applications. Their approach allows the prediction, not only for the full spectra of the atomic lines including fine multiplet structure, but also for the calculation of discrete energy levels of atomic particles. It was shown that the best result was obtained by using the experimental energy levels of atomic particles [27]. This approach guarantees a high degree of accuracy of the atomic line locations; without it the prediction would not include all lines. In short, this semi-empirical method allows parametric computations of approximately 4000 atomic lines for the atoms and ions N, N$^+$, O, O$^+$, C, and C$^+$. The database of these atomic lines by Surzhikov has been used in radiative gasdynamic calculations [24].
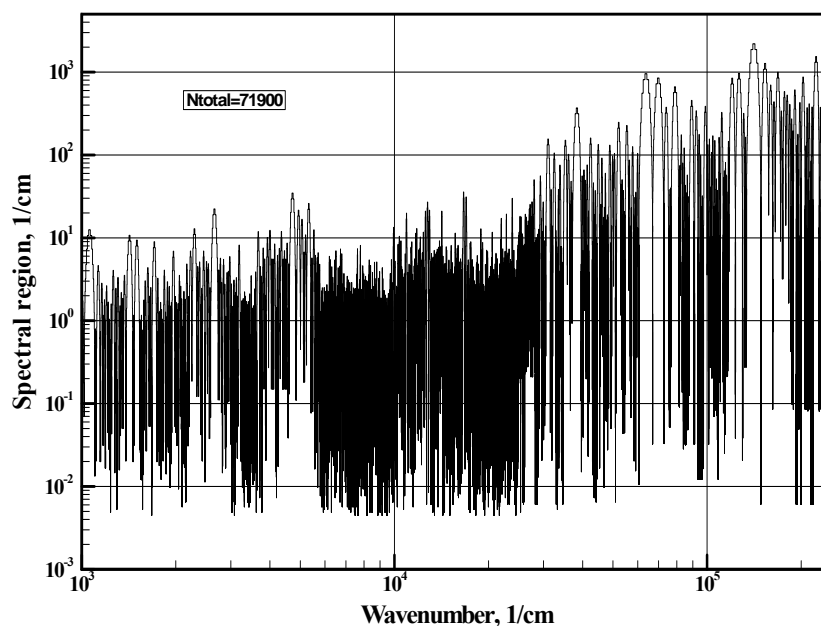

FIGURE 1. DISTRIBUTION OF SPECTRAL REGIONS USING THE INHOMOGENEOUS GRID VERSUS WAVENUMBER

The database of atomic lines for N, N$^+$, O, O$^+$ used in the present study are tabulated by wavenumber. Distribution of generated spectral regions for the line-by-line calculations is given in Fig. 1. A total of 71,900 spectral points is included in the diagram. In the spectral region from 10^3 to 2×10^4 cm^{-1}, a total of 1,500 atomic lines can be found. The most intense atomic line spectra are located in the ultraviolet and the vacuum ultraviolet domains (5.1×10^4 to 10^5 cm^{-1}) where quantum transitions take place between the excited states and the ground states. About 300 atomic lines are located in this spectrum; these lines are also known as the resonance atomic lines. For the present purpose, the minimal wavenumber increment for spectral calculations corresponds to the wavelength of the most significant lines. Figure 2 shows the cumulative function of the atomic-line distribution in the spectral region of practical interest.

The atomic lines calculation, including Stark line broadening, was tested in references 24 and 29. It should be noted that such calculation has demonstrated the result is no worse than using the classical data by Griem [30]. The Detailed information about molecular radiative processes is presented in references 14 and 15. Additional information with examples for spectral optical properties is presented in reference 31.
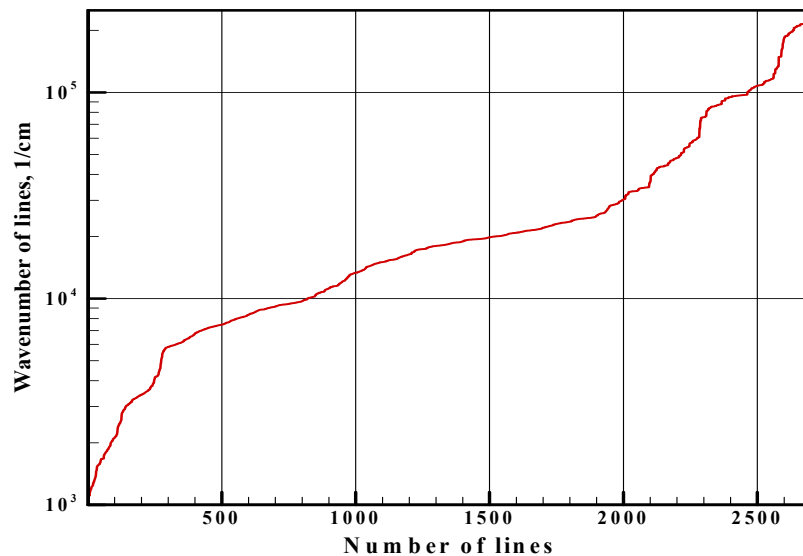

FIGURE 2. CUMULATIVE FUNCTION OF ATOMIC LINE DISTRIBUTION IN THE SPECTRAL REGION 1,000 < ΔΩ < 125,000 CM^{-1}.

Characteristics of Fire-II Flowfield

The coupled radiative gasdynamic results were obtained for trajectory points presented in Table 1. This table also contains computational results by Olynick et al [2] and Johnston et al [3]. The last three rows of the table contain data for radiation heat fluxes to the stagnation point with coupled (C), uncoupled (UC) assumption, and the radiation absorbed in optical windows of the radiometer $\alpha W_r(C)$. All parameters and their designations are duplicated from references 2 and 3.

The Fire-II space vehicle is simulated on a multi-block grid system, which consists of a total of four contiguous and perfectly matched grid blocks for the frontal face, afterbody, base, and wake regions. Figure 3a depicts the overall grid topology, and Fig. 3b highlights the clustered grid distribution for capturing the bow shock and the region immediately adjacent to the front surface of the capsule. A grid refinement study was also carried out and results will be presented latter in this paper. Typical global computational results obtained for the reentry space vehicle are presented in Figs. 4-10.

Figure 4 displays a composite representation of the longitudinal velocity component and translational temperature contours around the Fire II probe at the trajectory point at 1636 seconds. The numerical results are generated by the chemical kinetics model of Park [12]. The translational temperature reaches its maximum in the post shock layer and decreases to a value of 4,110 K over the afterbody. The temperature drops further in the wake region as anticipated. The freestream velocity enters the computational domain with a magnitude of 11.31 km/s and is decelerated by the bow shock. After two consecutive expansions at the outer edge of the front surface, corner of the base, and followed by a realignment compression; a recirculation zone exists in the base region.

The composite presentation of vibration temperatures of molecular nitrogen and oxygen is given in Figure 5. The only unusual part of the vibrational temperature contour is the heating of nitrogen by the recombination of nitrogen atoms.

The high vibrational temperature of N_2 and O_2 molecules has a specific property of the expanding flows behind any space vehicle at non-equilibrium conditions. It is fully understood that the heterogeneous kinetics and kinetics of recombination near the leeward surface is questionable locally. However, such description of gasdynamic parameters and assumptions concerning these non-equilibrium regions are commonly used in the literature. In previous publications we have used the opposite assumption with the absence of any catalytic properties [32]. Nevertheless, the phenomenon under consideration is significant for radiative and convective heating of the afterbody surface of space vehicles (and it should be considered more in detail), but it is insignificant for the radiative convective heating to the front shield of a space vehicle.

As an illustration for the importance of including the atomic lines for radiative heat transfer, a series of computations were carried out with the Park kinetic model for the Fire II at t=1636 s. The rates of dissociation reactions were calculated by assuming local thermal equilibrium (LTE), namely all temperatures for dissociation rates were set to equal the translational temperature.

The translational temperature and the vibrational temperature of molecular nitrogen, oxygen, as well as nitric oxide are depicted in Fig. 6a for trajectory point t=1636 s. The well-established thermally equilibrated behavior shortly downstream of the bow shock is clearly shown. The translational and vibrational temperature in the shock layer of molecular nitrogen, oxygen, and nitric oxide reach an equilibrated value of 11,200 K. In Fig. 6b, the eleven chemical species of high-temperature air along the stagnation streamline also exhibit a familiar pattern and agree well with all published computational results [3].

The numerical investigation of radiative gasdynamic processes for the Fire-II reentry reveals a high sensitivity to the radiating gasdynamic field. The sensitivity is not only associated with the models of chemical and physical kinetics, but also with the computational grids and their topology. This behavior can be explained by the strong dependence of the characteristics of the ionization processes to the flowfield condition. To illustrate this fact, the simulated axial temperature and species concentration distributions by two different computational grids are presented in Figure 6.

In Figure 7, the drastically different spectral radiative flux intensity wavenumber profiles calculated with/without atomic lines stands out at the stagnation point of the Fire II probe. Although the spectral intensity appears as multiple Dirac delta functions at a specific wavenumber, the number of the spectral lines within the pertaining spectrum is huge. As a consequence, the magnitude of the cumulative functions over the full spectrum becomes significant.

The cumulative function can be formally defined for a spectral region $\Delta\omega = \omega - \omega_{\min}$ by $Q_{\Delta\omega} = \int\limits_{\omega_{\min}}^{\omega} W_{w,n,\omega} d\omega$. If $\omega = \omega_{\max}$ then the cumulative function is the total integrated radiative flux in a given spectrum and it has the physical units of W/cm². In essence, this function reveals the contribution to the integrated radiative heat flux within a specific spectral region. From this result, it is shown that the contribution to radiative exchange at low wavenumber is derived from the bound-bound transitions, free-free transitions and the vibrational molecular bands. In the spectral region of 2×10^4 - 8×10^4 cm^{-1}, the radiation is mostly by emission of the visible and ultraviolet bands of diatomic molecules. In all, within the frequency spectrum from 1000 to 125,000 cm^{-1}, the cumulative spectral lines are 71,900 in number.

The increased spectral radiative heat flux by including the atomic lines at the stagnation point is depicted in Figure 8. In this presentation, both computations including atomic lines or not are given. All the calculated radiative fluxes are generated at the trajectory stage of t=1636 s for the Fire II probe. The atomic lines in the infrared regions, from 1000 to 1.4×10^4 cm^{-1}, in wavenumber or from 0.71 to 10 μm in wavelength, contribute more than 10 W/cm² to the integrated radiative flux. The atomic lines in the visible (1.4×10^4 to 2.5×10^4 cm^{-1}) and ultraviolet spectrum ranges also contribute significantly to the increase in the radiative flux. For the spectrum up to 10^5 cm^{-1}, more than 5 times the radiative flux is contributed by the atomic lines.

Figure 9 presents the calculated heat transfer rates by radiation, conduction, and convection at the stagnation point at the t=1636 s trajectory point. The radiative heat exchange, including the atomic lines, is only performed over the front face of the Fire II probe by the half moment method with Park's kinetics model and the LTE assumption. The magnitude of the radiative heat transfer rate is around 50% of the total rate of heat transfer on the front surface.

TABLE 1. TRAJECTORY PARAMETERS OF FIRE-II REENTRY VEHICLE AND SOME NUMERICAL SIMULATION RESULTS FROM REFERENCES [2,3]

t, s	1634	1636	1637	1639	1640	1643	1644	1645	1648	1651
$\rho_\infty \cdot 10^{+7}$, g/cm^3	0.372	0.857	1.47	2.41	3.86	7.80	10.2	13.2	30.0	60.5
p_∞, erg/cm^3	20.8	51.7	96.2	167.4	281.4	617.9	822.6	1079.7	2298.9	4393
T_∞, K	195	210	228	242	254	276	281	285	267	253
T_w, K	615	810	1030	1325	1560	640	1100	1520	1560	1060
V_∞, km/s	11.36	11.31	11.25	11.14	10.97	10.48	10.19	9.83	8.3	6.19
R_n, cm	93.5					80.5			70.2	
$\alpha\, W_r$ [2] W/cm^2	~18	60.	125.1	207.5	290.	357	324	237	52.1	11.5
W_r (UC) [3] **W/cm²**	31.3	106	217		609	713		354	51.4	
W_r (C) [3] **W/cm²**	27.2	86.1	169		445	540		303	43.1	
$\alpha\, W_r$ (C) [3] /cm²	19.7	62.4	120		296	344		184	24.6	
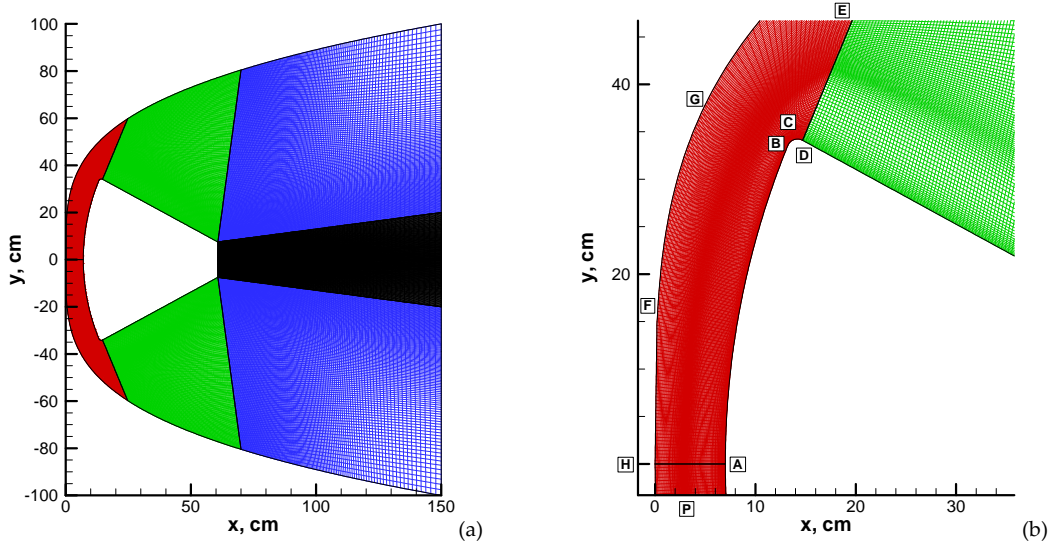
FIGURE 3. GRID TOPOLOGY OF (a) MULTI-BLOCK AND (b) CLUSTERED GRID-POINT DISTRIBUTION IN SHOCK LAYER
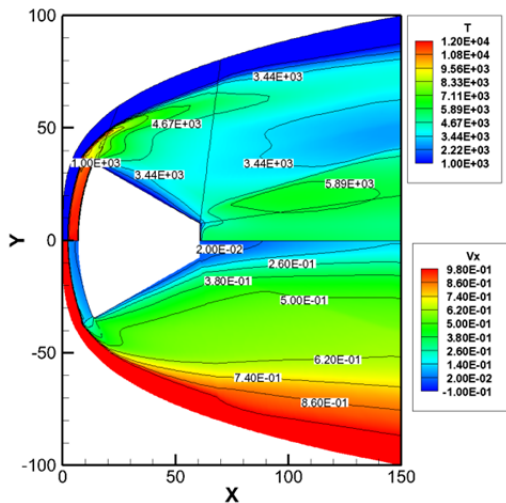
FIGURE 4. RESULTS OF LONGITUDINAL VELOCITY (KM/S, BOTTOM) AND TRANSLATIONAL TEMPERATURE (K, TOP) AROUND FIRE-II AT t=1636 s BY PARK KINETIC MODEL [12]; X AND Y (CM)
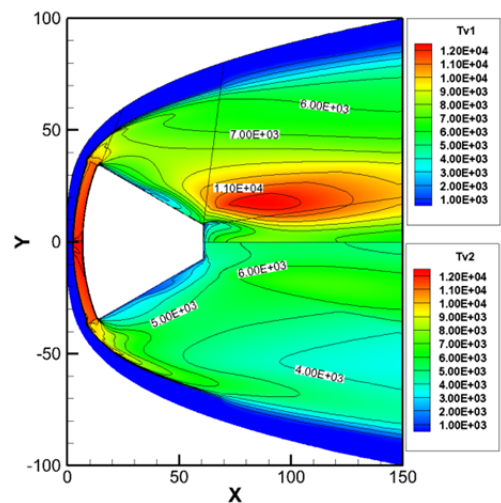
FIGURE 5. SOLUTIONS OF VIBRATIONAL TEMPERATURE N2 (K, TOP) AND O₂ (K, BOTTOM) AROUND FIRE-II AT t=1636 s USING PARK KINETIC MODE; X AND Y (CM)
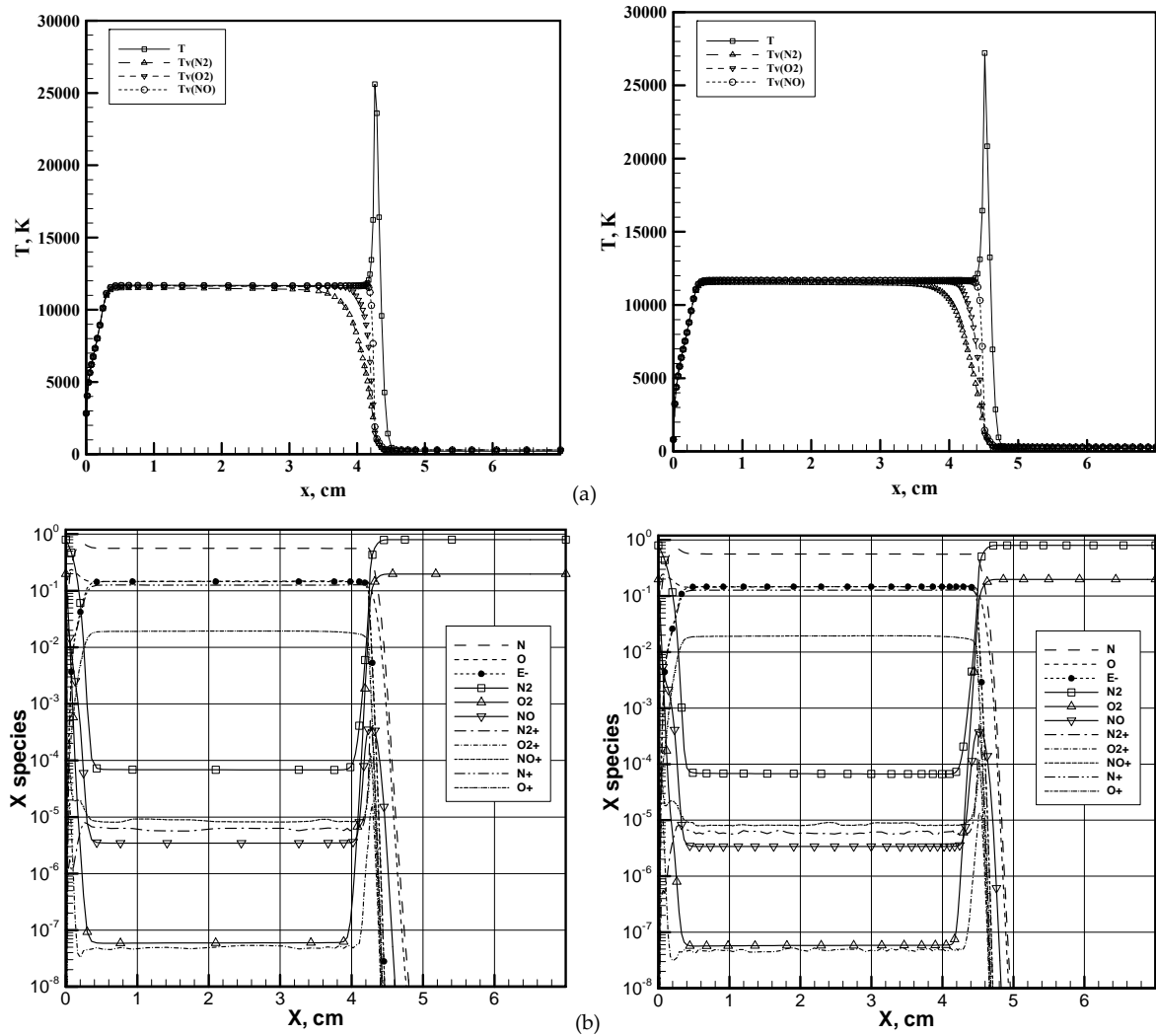
FIGURE 6. DISTRIBUTIONS ALONG STAGNATION STREAMLINE OF (A) TRANSLATIONAL AND VIBRATIONAL TEMPERATURES ON (61X69) MESH SYSTEM AND (B) SPECIES CONCENTRATIONS ON (121X137) MESH SYSTEM FOR FIRE-II AT t=1636 s.
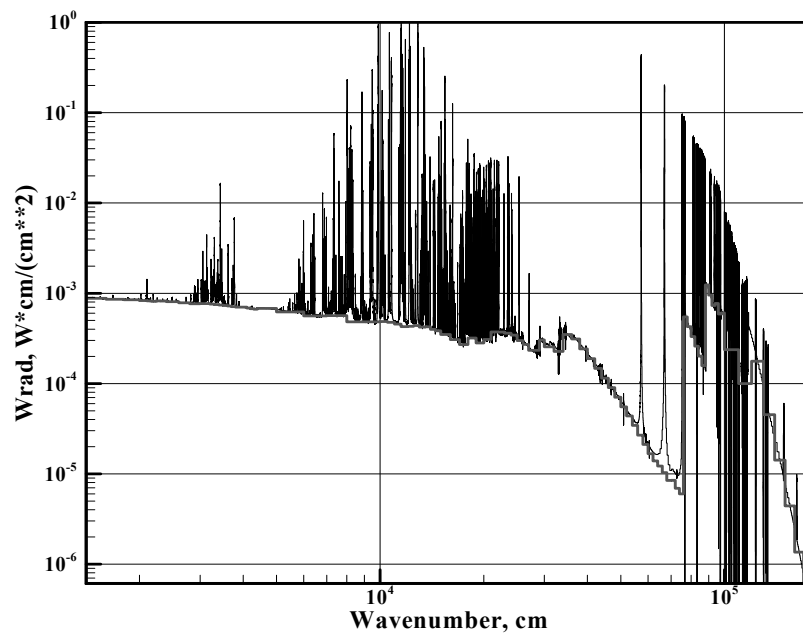

FIGURE 7. SPECTRAL RADIATIVE HEAT FLUX AT STAGNATION POINT FOR FIRE-II AT t=1636 s; BOLD CURVE HAS NO ATOMIC LINES, THIN CURVE HAS ATOMIC LINES.
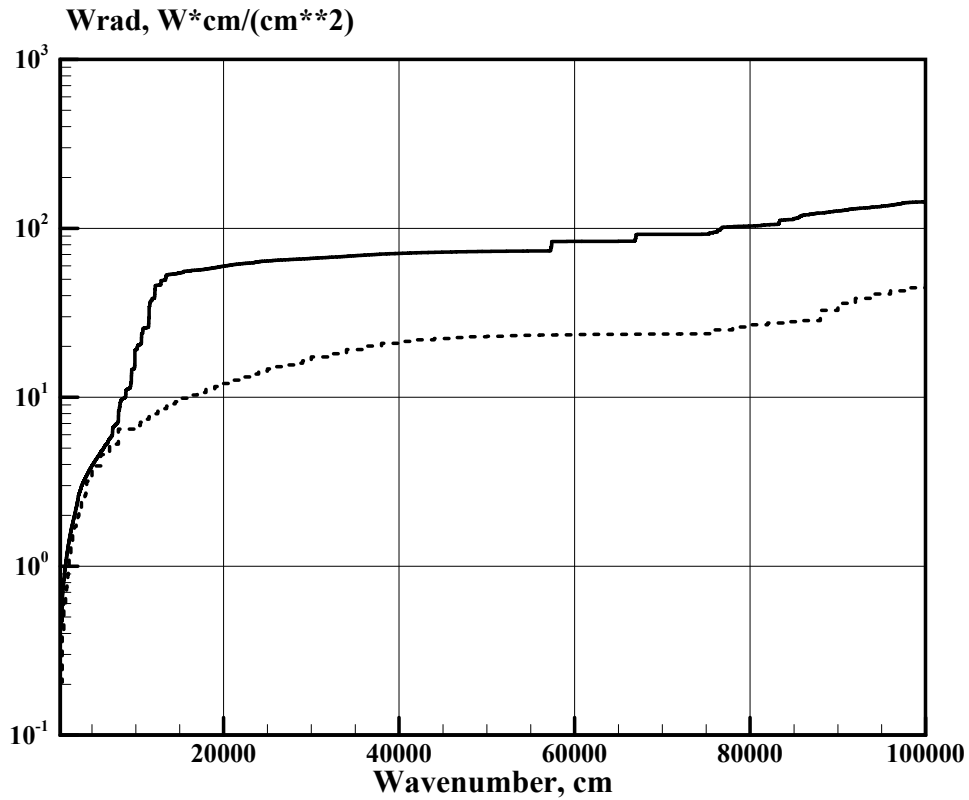
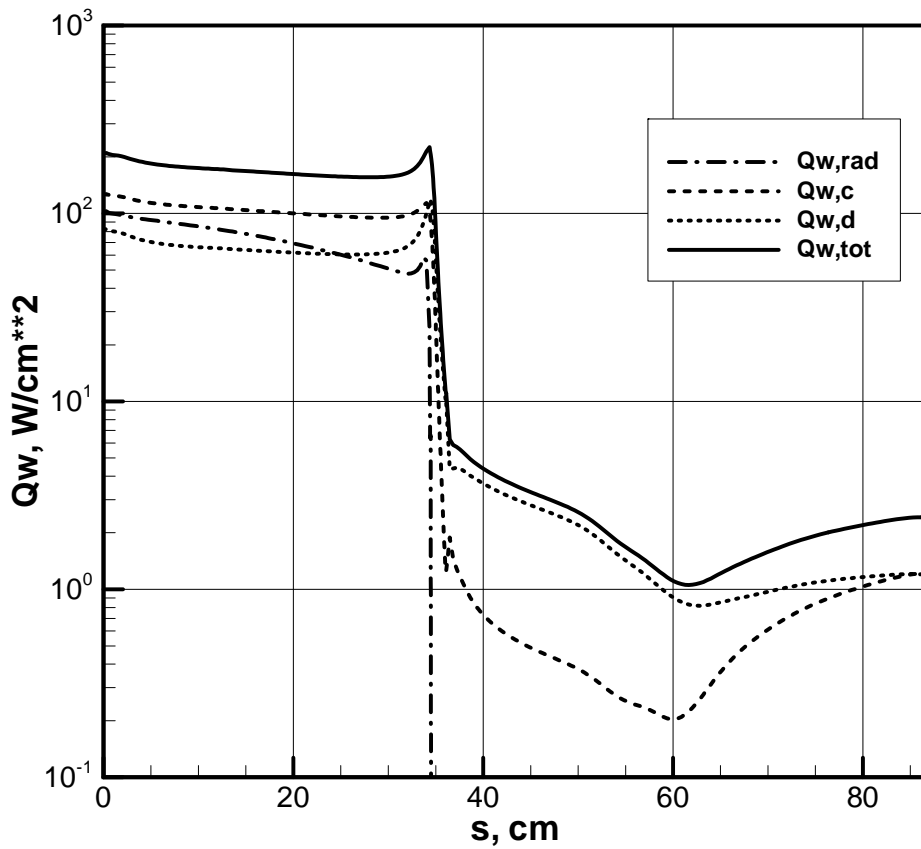**Wrad, W*cm/(cm**2)**

FIGURE 8. CUMULATIVE FUNCTION OF SPECTRAL RADIATION HEAT FLUX AT STAGNATION POINT OF FIRE-II AT *t*=1636 s; DASHED CURVE HAS NO ATOMIC LINES AND THIN CURVE HAS ATOMIC LINES

FIGURE 9. DISTRIBUTION OF CONVECTIVE (HEAT CONDUCTIVE (*C*) AND DIFFUSION (*D*) COMPONENTS) AND RADIATION HEAT FLUXES WITH ATOMIC LINES ALONG SURFACE OF FIRE-II AT *t*=1636 s.
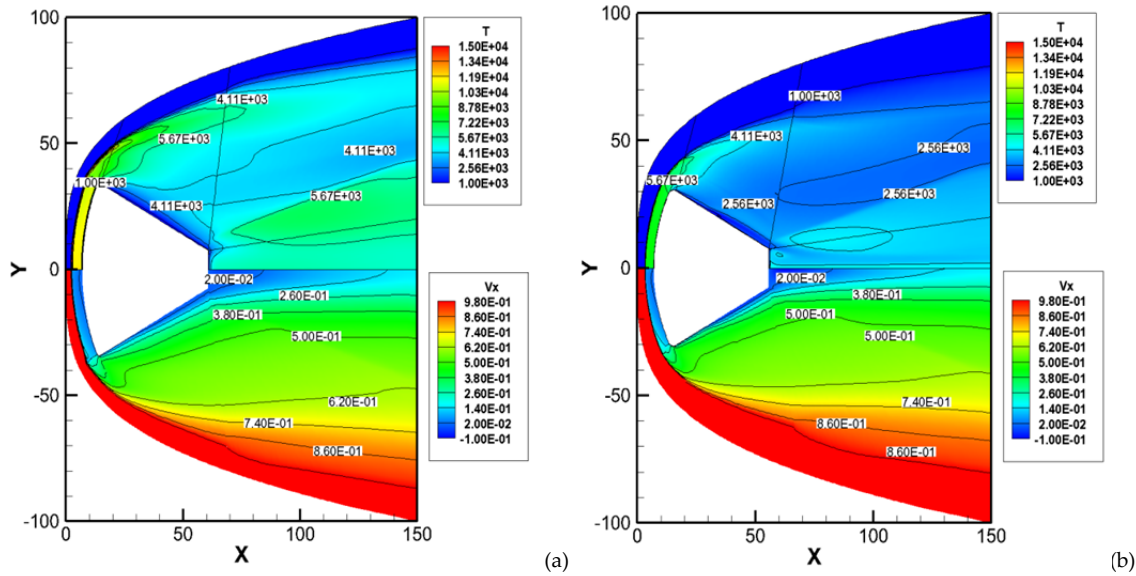
FIGURE 10. TEMPERATURE AND LONGITUDINAL VELOCITY AT T=1634 S (*a*) AND t=1648 s (*b*) USING DUNN-KANG KINETIC MODEL AND LTE CONDITION; X AND Y (CM)

Numerical Simulation Results for Different Chemical and Physical Kinetics Models

Two general objectives were pursued by the following comparative computations. The first objective is to determine the contribution of atomic lines over the full spectra to the total radiative heating of the reentry probe. The second goal is to assess the effect of radiation-gasdynamic coupling and different vibration relaxation by using different physical kinetic models. The final verification of the present numerical results is achieved by comparison with experimental data and computational results available in the open literature.

The general censuses by examining the flight data of the reentering Fire II are that the radiating flow transitions from nonequilibrium to equilibrium conditions with a significant lag between the characteristic transition during the trajectory stages from 1634 to 1651 seconds [2,3]. Two flowfields around the probe at 1634 and 1648 seconds are generated by the kinetics model of Dunn and Kang [11] and by assuming the LTE condition. In Figure 10, the detailed difference in global flowfield formation is of course not discernible by comparing the velocity and temperature fields at these conditions. The velocity contours at the two stages are nearly identical, but the wake region is retracted by the reduced standoff distance of the bow shock wave. At the same time, a lower translational temperature is noticed in the aerodynamic shadow during the later stage of the reentry trajectory. The difference is 2,560 versus 4,110 K from the earlier stage of reentry. At t=1634 s, the flowfield actually reveals that the heat release by the recombination process is not yet dissipated.

The radiation simulation is generated by the coupled and uncoupled radiation-gasdynamics formulation in the framework of the multi-group spectral model. This multi-group model consists of 97 spectral subgroups. One example of such a model is depicted in Figure 7 by a bold, Dirac delta function curve. About 70% of these spectral groups contain atomic lines, and the total absorption coefficients of each group are predicted by integration of the synthetic spectrum of absorption. Then the precise line-by-line calculations of radiative heat transfer including over 71900 inhomogeneous wavenumber grids are performed by the half-moment method. All gasdynamic variables, thermodynamic states, and species concentrations are obtained by solving the gasdynamics equations and the line-by-line spectral calculations. The computational results of the translational and vibrational temperatures of molecular nitrogen, oxygen, and nitric oxide are depicted in the following figure along the stagnation streamline of the Fire II probe.

Nine different conditions of the reentry trajectory of the Fire II probe at 1634, 1636, 1637, 1639, 1640, 1643, 1644, 1645, and 1648 seconds are simulated to investigate the effects of kinetic modeling to the key dependent variables of the flowfield, thermodynamic properties, and finally the radiative heat exchange rates. The chemical kinetics models by Park [12] and Dunn and Kang [11] are selected for a series of computational investigations. These models have been successfully applied into aerophysics research over many years, and therefore they can be

considered to be fully validated. Unfortunately, at the same time, the empirical nature of these models requires additional modifications for the physical fidelity of the computational simulations.

Effects of Biased Dissociation to Vibrational Relaxation

One of the uncertainties of these models is the vibrational relaxation in the presence of dissociation. To address this issue, two models of vibrational degrees of freedom are implemented in the computational procedure. In the first case, the molecular distributions of vibrational states are assumed to be Maxwell-Boltzmann. The reaction rates of dissociation are calculated by the LTE model. In the second case, the Treanor-Marrone model of non-equilibrium dissociation is used [13]. This group of comparative studies is summarized by Figs.11 a-h. The Dunn and Kang kinetics model was used in this series of results.

The biased dissociation to vibration relaxation using the kinetics model of Dunn-Kang reveals a consistently greater standoff distance of the shock layer than the LTE assumption. Independent of the different assumptions used for the simulations, the maximum standoff distance of 5.25 cm is observed at t=1634 s. The minimum counterpart is recorded at 3.6 cm when t=1648 s at the last stage of the Fire II trajectory simulated. As a consequence, the equilibrated condition between vibrational and translational temperature is reached sooner in the shock layer. In general, the spike in translational temperature in the immediate post shock region is higher with the Treanor-Marrone model than that of LTE, which is understandable that the former is based on a realistic energy transport process. During the fully nonequilibrium part of the reentering trajectory (t<1637 s), the models of nonequilibrium dissociation significantly alter the vibrational temperatures with a consequence of changing radiative emission.
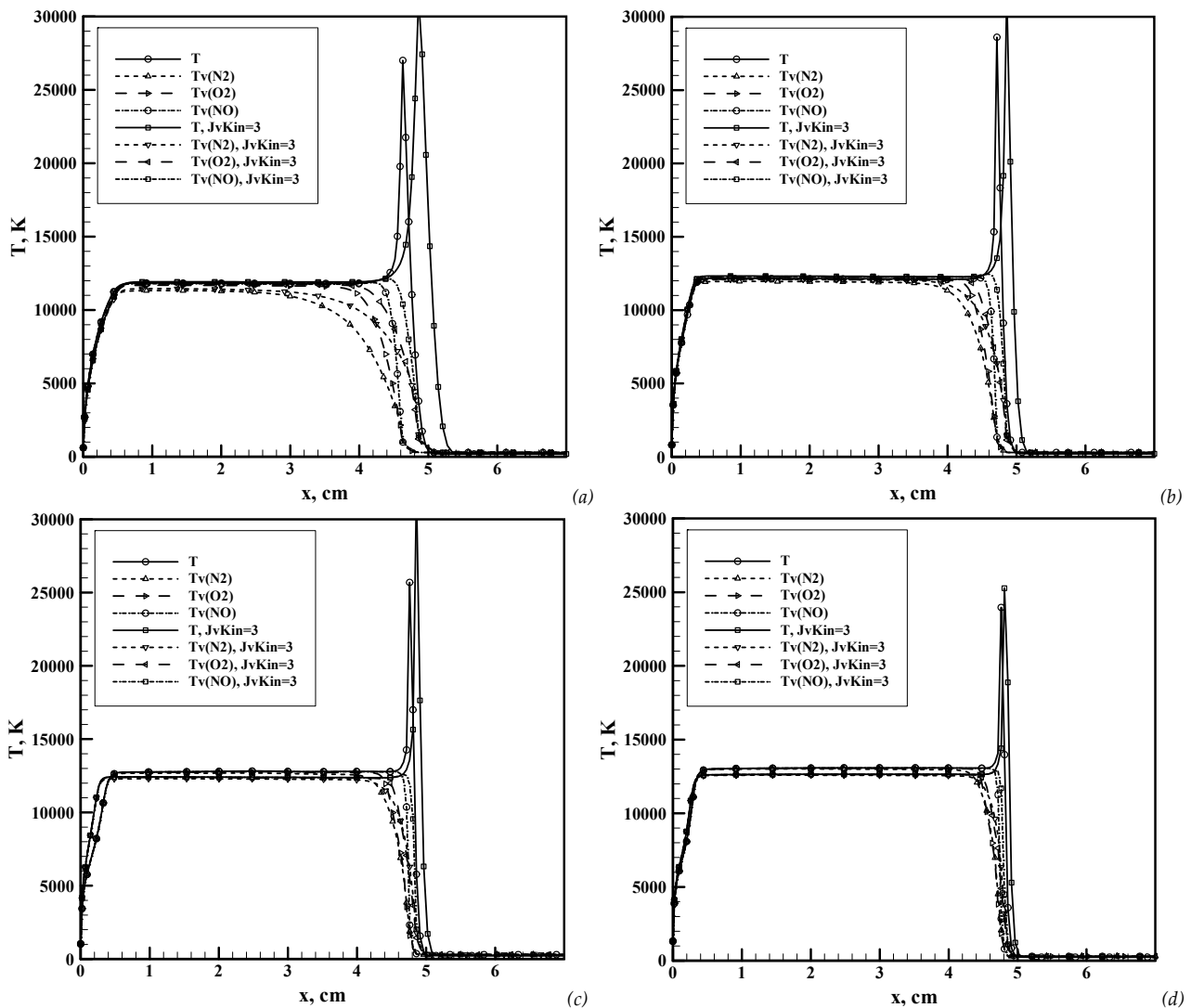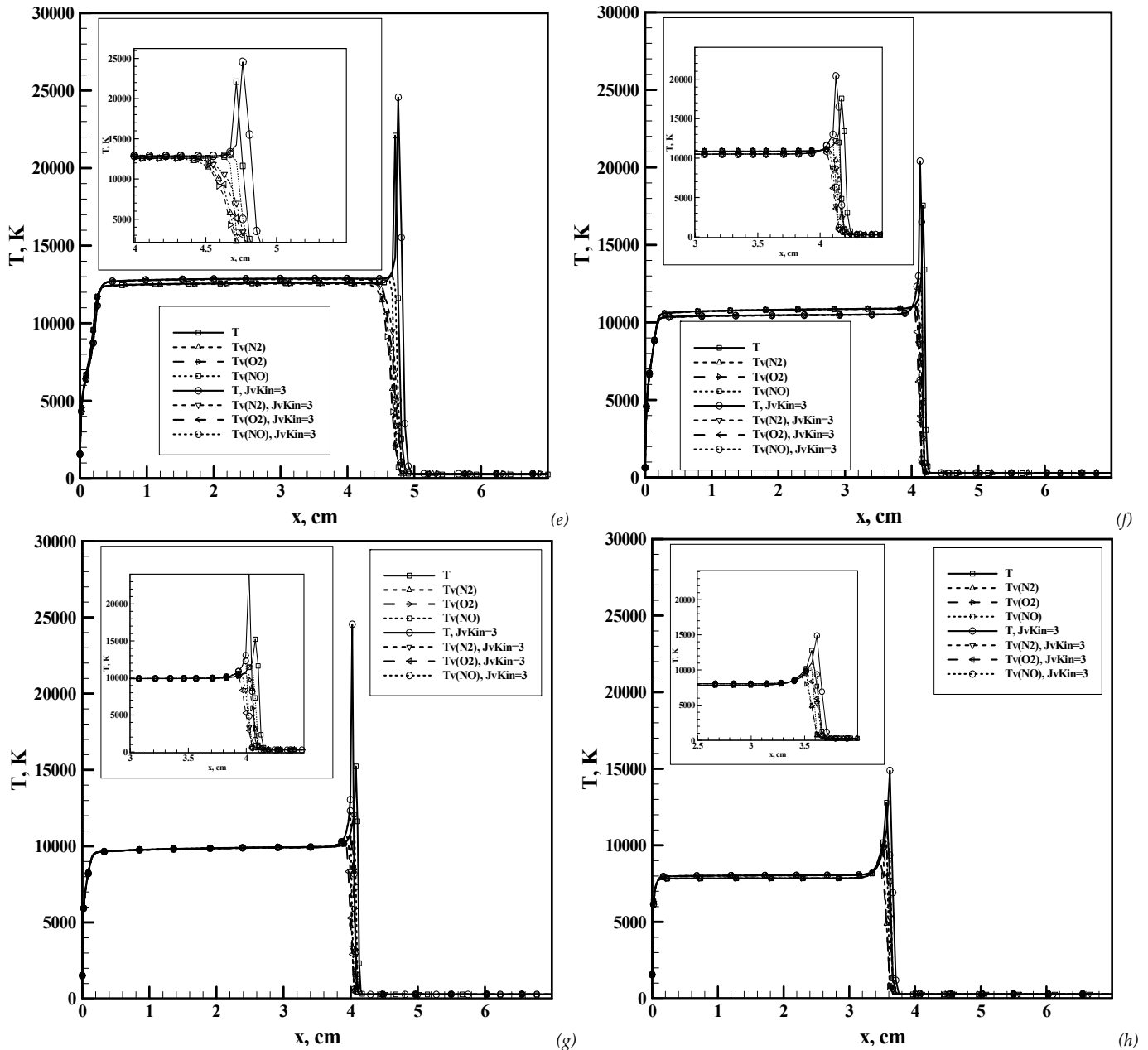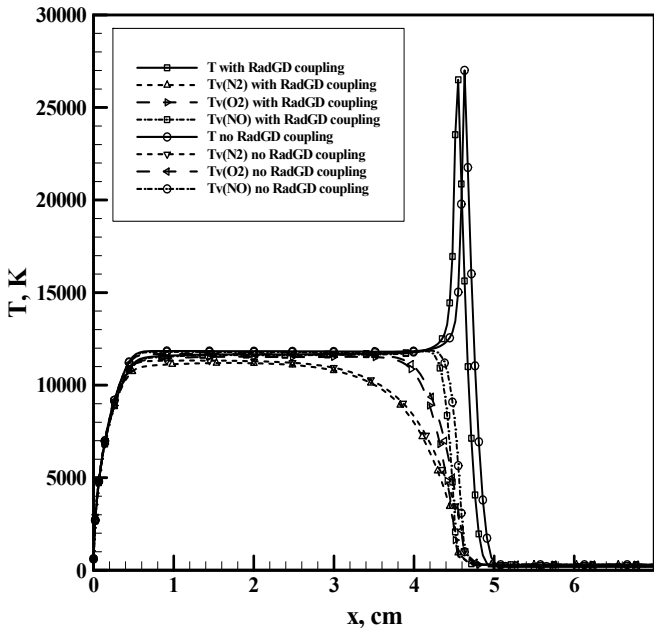
FIGURE 11.   DISTRIBUTIONS OF TRANSLATIONAL AND VIBRATIONAL TEMPERATURES ALONG THE FORWARD STAGNATION
LINE FOR TWO MODELS OF NON-EQUILIBRIUM DISSOCIATION (JVKIN=0 – LTE, JVKIN=3 [13]) WITHOUT GASDYNAMIC–
RADIATION COUPLING AT (a) *t*=1634 s, (b) *t*=1636 s, *(c)* *t*=1637 s, *(d)* *t*=1639 s, *(e)* *t*=1640 s, *(f)* *t*=1643 s, *(g)* *t*=1645 s , *(h)* *t*=1648 s. ZOOMED
PARTS OF THE FIGURES SHOW TEMPERATURE DISTRIBUTIONS BEHIND SHOCK WAVE

Nonequilibrium/Equilibrium Radiation by LTE

The coupling effect between the gasdynamics and radiative process for the Fire II reentry is presented in Figs.12a-h. In a way, it reflects whether radiation is in an equilibrium or nonequilibrium condition with the gasdynamics. For this series of comparative results, the reaction rates of dissociation are obtained by assuming the LTE condition in the chemical kinetics model of Dunn-Kang.

Taking into account the radiation gasdynamic coupling leads to decreasing temperatures in the shock layer at the earlier stage of the reentering trajectory. Figures12 a-h shows the maximum differences between temperatures in the shock layer. The computational results demonstrate the 'classical' results of the coupling effect; namely the standoff distance of the bow shock, the temperature within the shock layer decrease, and the temperature in the boundary layer increases. One can also observe the effect of radiation gasdynamic coupling becoming weaker during the later trajectory points, $t > 1640$ s.
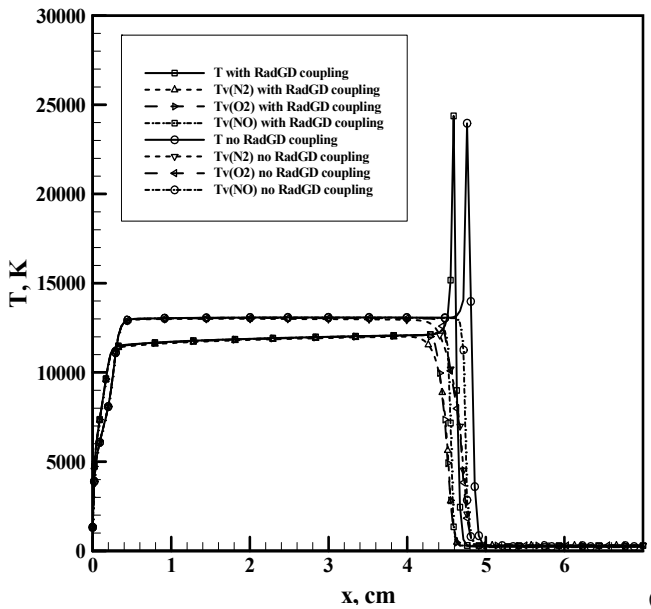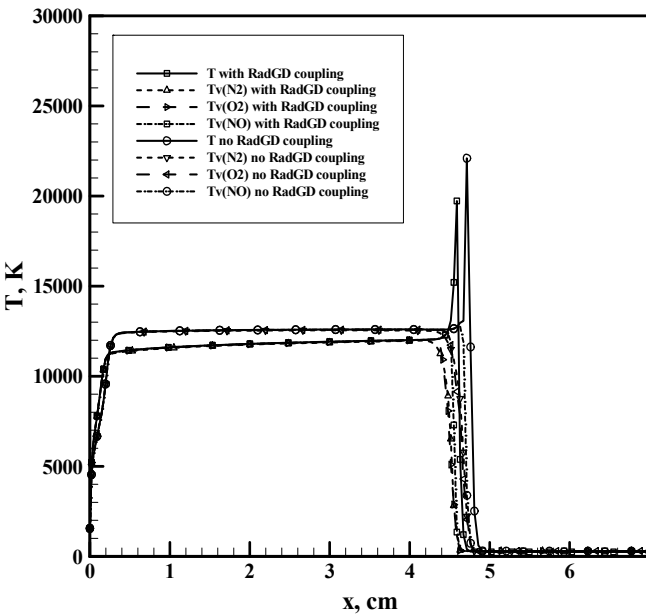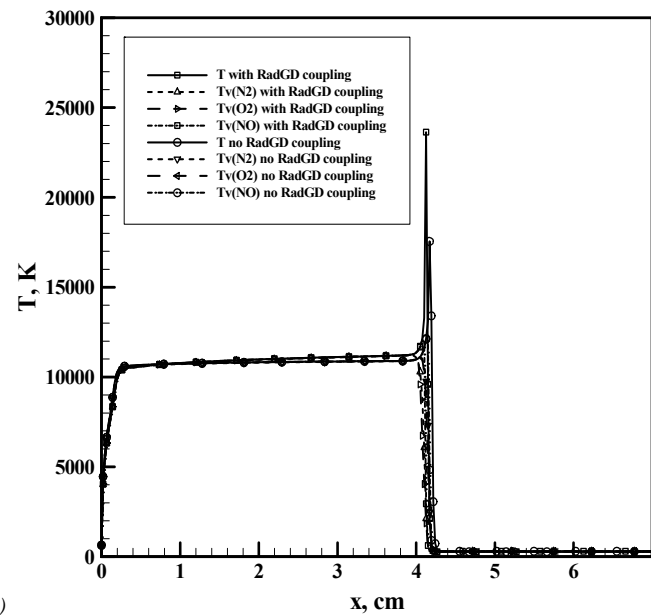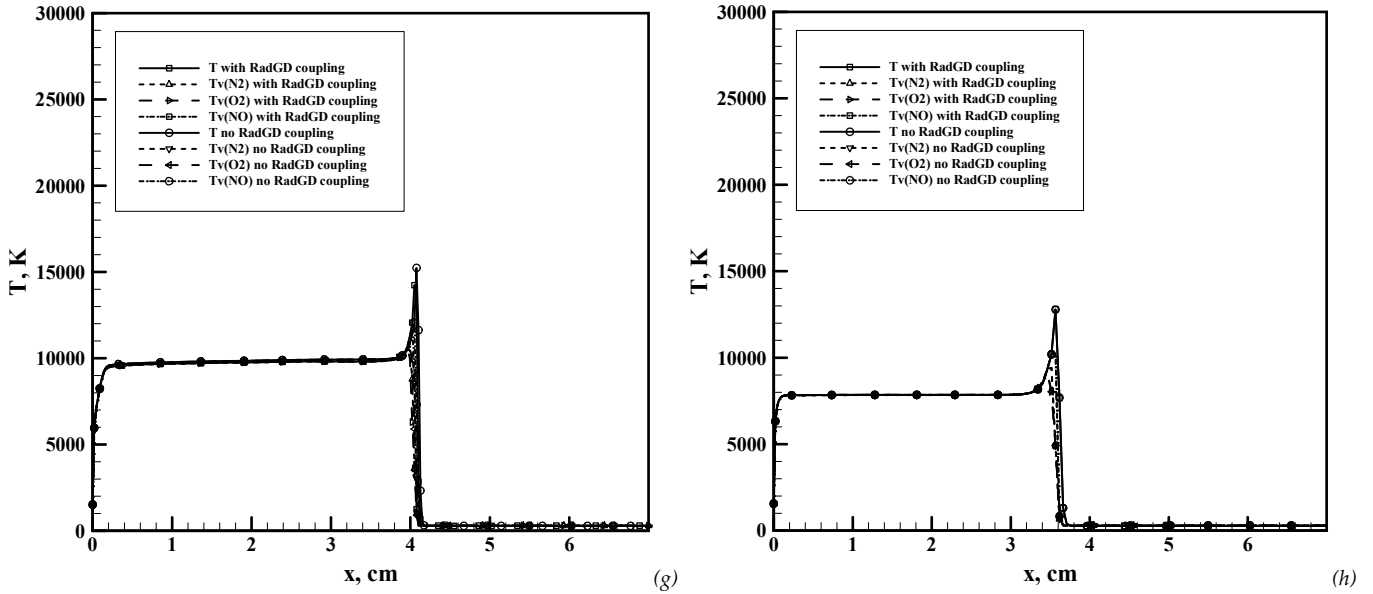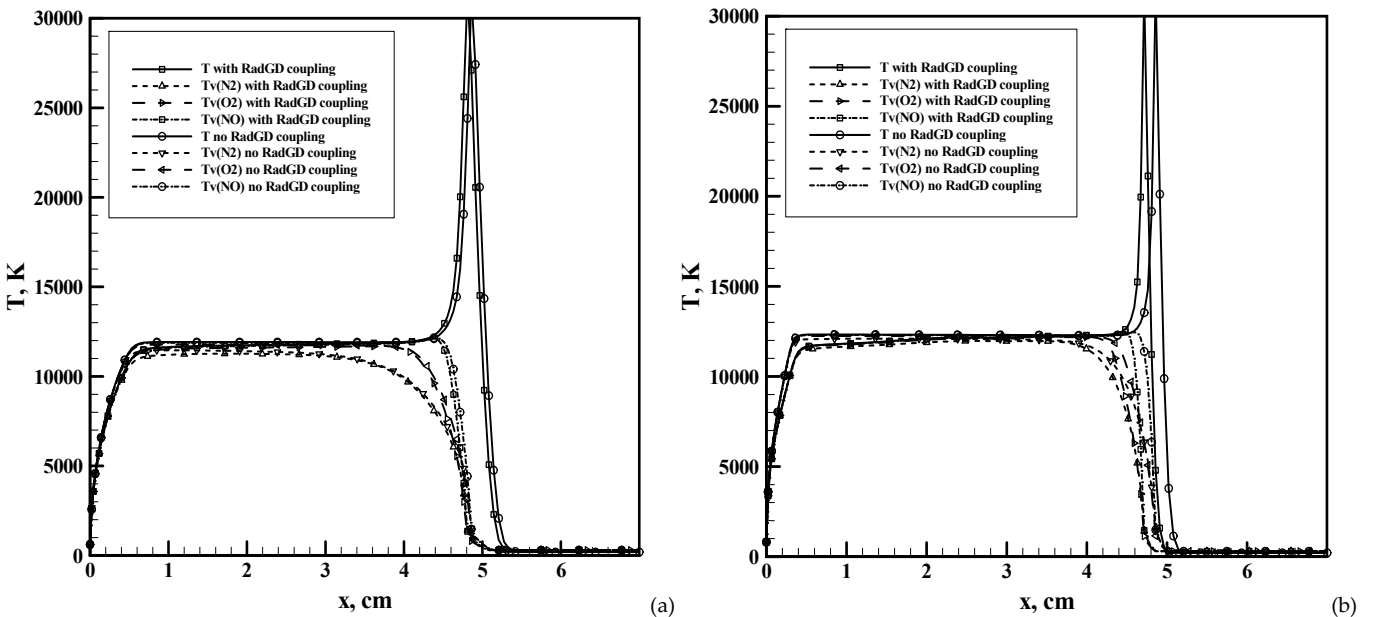
(a)
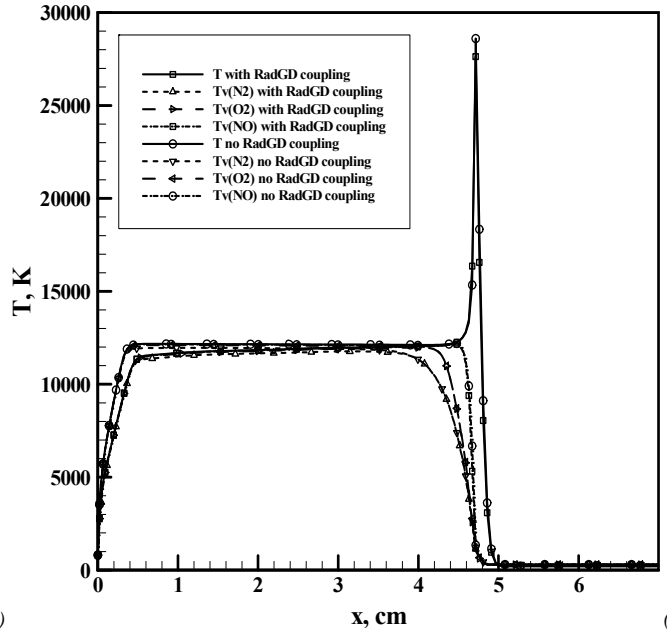
(b)
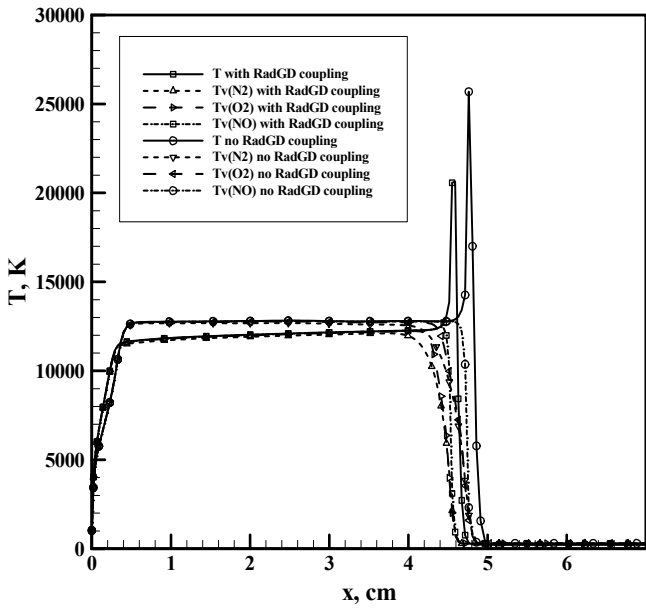
(c)

(d)

(e)

(f)

FIGURE 12. DISTRIBUTION OF TRANSLATIONAL AND VIBRATIONAL TEMPERATURES ALONG STAGNATION STREAMLINE USING DUNN-KANG KINETIC MODEL AND LTE CONDITION WITH/WITHOUT GASDYNAMICS-RADIATION COUPLING *(a)* at *t*=1634 s, *(b)* *t*=1636 s, *(c)* *t*=1637 s, *(d)* *t*=1639 s, *(e)* *t*=1640 s, *(f)* *t*=1643 s, *(g)* *t*=1645 s, *(h)* *t*=1648 s.

Nonequilibrium/Equilibrium Radiation with Dissociation Biased

To further understand the coupling of the gasdynamic with radiative processes, a more realistic vibrational model by Treanor-Marrone [13] is used instead of the assumption of LTE for the following study. The results are depicted in the Figures 13a-h.

A consistent and large difference between the coupled gas dynamics and radiation and uncoupled results is displayed. The high physical fidelity modeling of the nonequilibrium dissociation model highlights the nonequilibrium radiative phenomenon. The decreased standoff distance of the nonequilibrium radiation simulations exhibits a similar and nearly identical magnitude as observed in the previous calculations. The nonequilibrium radiation reduces the standoff distance, and the effect is more pronounced in the later stage of reentry. The maximum disparity is around 10.5% at 1640 s. Meanwhile the equilibrated temperature of the coupled results along the stagnation streamline is also elevated at the later stage of reentry and reaches a value of more than 1000 K. The identical effects of a thinner standoff distance of the radiative cooling of the blunt nose are also observed for the Stardust reentry simulation [10].
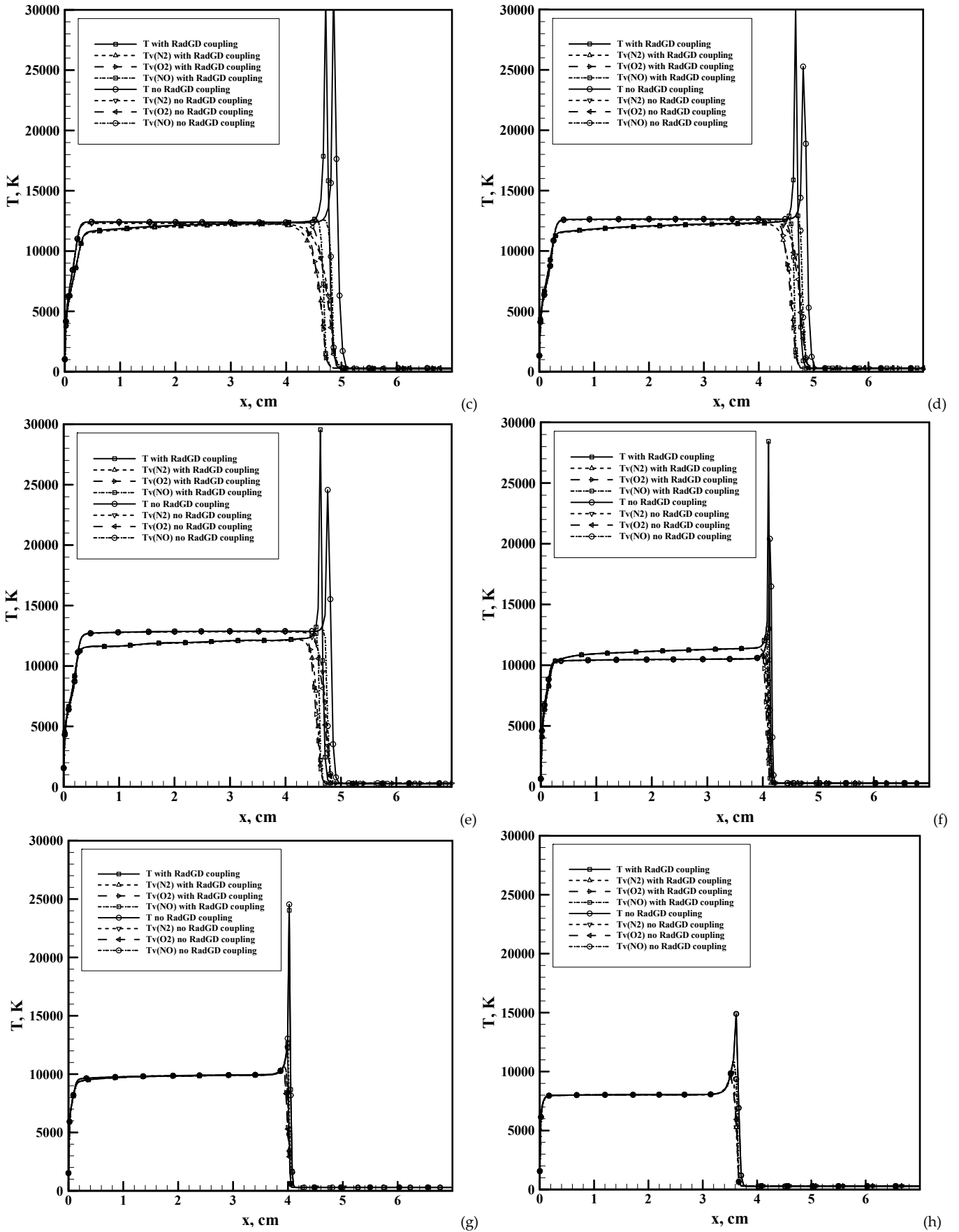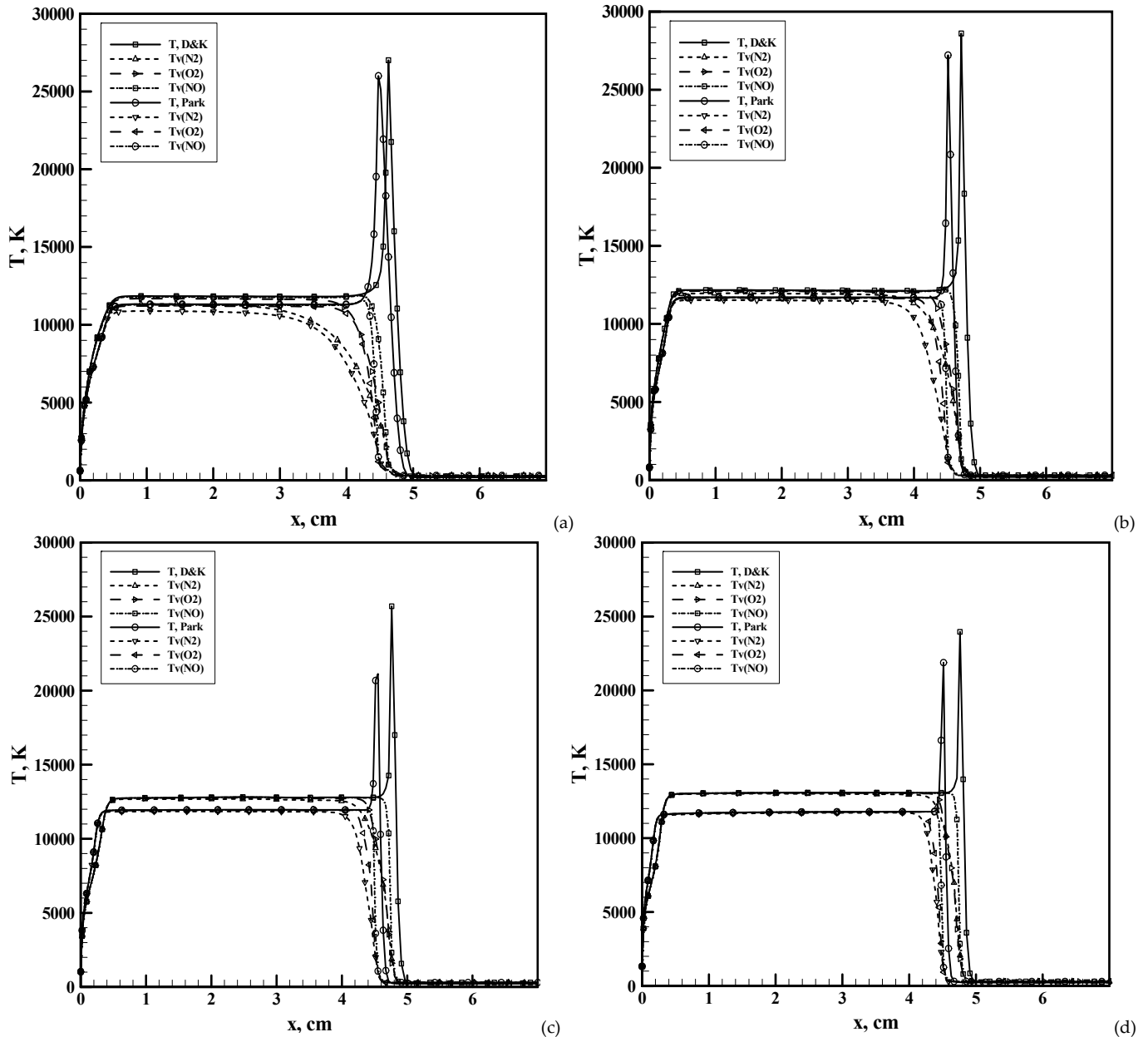
FIGURE 13. DISTRIBUTION OF TRANSLATIONAL AND VIBRATIONAL TEMPERATURES ALONG STAGNATION LINE USING KINETIC MODEL OF NONEQUILIBRIUM DISSOCIATION, WITH/WITHOUT GASDYNAMICS-RADIATION COUPLING AT *(a) t*=1634 s, *(b)t*=1636 s, *(c) t*=1637 s, *(d) t*=1639 s, *(e) t*=1640 s, *(f) t*=1643 s, *(g) t*=1645 s , *(h) t*=1648 s.

Nonequilibrium Radiation by Two Kinetics Models

The comparison of the kinetics models by Dunn-Kang [11] and Park [12] is displayed in Figures 14a-h. For this series of calculations, the LTE assumption is applied into both the coupled interdisciplinary gasdynamics and radiation equations.

In short, the difference in temperature profiles generated by the two models along the stagnation streamline is quite significant. The standoff distance from the model by Dunn-Kang is slightly greater than that of Park by a maximum ratio of 5%. On the other hand, the predicted equilibrated temperatures from the model of Park are 1,000 to 1,200 K lower during the earlier stages of reentry (up to *t*=1644 s). However, the predicted temperatures in the shock layer are essentially identical during the later stages of reentry. In summary, the difference in predicted results between the two chemical kinetics models is of the same order-of-magnitude as the difference produced by the models for nonequilibrium vibration.

It should be stressed, in summarizing results of the influence of the chemical kinetics and physical kinetics models (non-equilibrium dissociation) that the observed temperature differences of 1000 K are quite significant for a correct prediction of radiative heating.
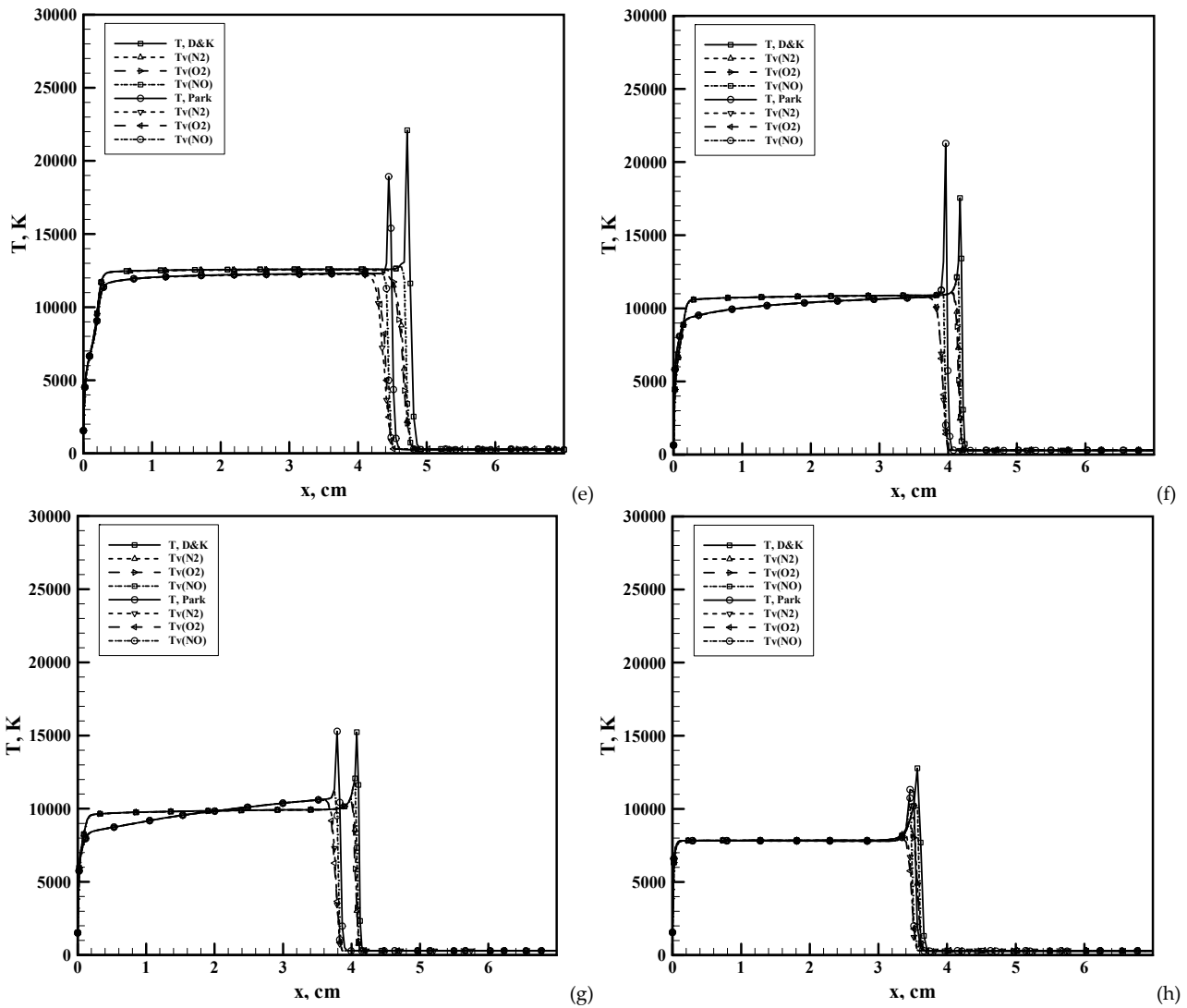
FIGURE 14. COMPARISON OF KINETIC MODELS [11, 13] IN LTE FOR TRANSLATIONAL AND VIBRATIONAL TEMPERATURES ALONG STAGNATION STREAMLINE WITHOUT GASDYNAMIC-RADIATION COUPLING AT *(a)* t=1634 s, *(b)* t=1636 s, *(c)* t=1637 s, *(d)* t=1639 s, *(e)* t=1640 s, *(f)* t=1643 s, *(g)* t=1645 s, *(h)* t=1648.

Radiation with Atomic Lines

Finally all calculations were repeated with and without radiation-gasdynamic coupling as well as with and without the atomic lines for radiative energy transfer. In here, the coupling of radiation-gasdynamics is viewed as whether an equilibrium state existed or not between radiation and the chemically reacting flowfield. An assessment by including the atomic lines for numerical simulations is one of the key objectives of the present study. For this model, the data collected by Cauchon via a calorimeter [1] and further organized by Johnston, Hollis, and Sutton [3] become the cornerstone of the present verification process. These excellent data were collected and deduced by different techniques and had a difference in peak heating rates on the order of 50 W/cm² and a time line disparity of 2 seconds. The small discrepancy is an impressive 4% error. As an expanded comparative study, the computational results by the GIANT and LAURA codes in a published article by Olynick [2] also lend credence to the present investigation.

Figures 15 and 16 show integrated results of the predicted values of convective and radiation heat fluxes along Fire-II trajectory for different physical and chemical kinetic models. The differences in predicted values are highlighted by taking into account the radiation gasdynamic coupling and the spectral atomic lines. Experimental data and all known computational results are also presented in these figures [1-3].

Figure 15a exhibits the contrast between the total heat transfer rates at the stagnation point with/without the

contribution of the atomic spectral lines. For these series of computations, the chemical kinetics model of Dunn-Kung is adopted. The standards for comparison are established by the data bases of Cauchon [1] and are correlated by Johnston et al [3]. The experimental data indicate heat transfer rates of 150 W/cm² at the initial descending stage and a peak heating load of 1140 W/cm² at 1644.5 s (the data by Cauchon is designated by the filled black square symbols). The total heat transfer rates reduce to a value less than 320 W/cm² at the last measured stage, t=1652s. The present computational results agree very well with data over the entire trajectory by Cauchon. This conclusion holds independently from the two possible nonequilibrium dissociation approximations for radiation computations. Equally important, the difference between the total heat transfer rates with/without the atomic spectral lines is 150 W/cm² at the peak heating load, radiative heating without atomic lines can be estimated from Fig. 15b for t=1644.5 s. Finally, the present predicted heat transfer rates with and without the contribution of the atomic spectral lines bracket the results from the LAURA and GIANT codes, presented by Olynick et al [2].

The radiative heat fluxes by either the LTE or the Treanon-Marrone models are included, and there is a smaller difference in the numerical results than from the predictions omitting the atomic spectral lines. As a reference for the relative magnitudes of total heat flux to the nonequilibrium radiative flux, the correlated data by Johnston, designated by the yellow filled square symbols are included. The radiative heating calculations at the seven trajectory points by Olynick et al [3] are also inserted and denoted by the black circle symbols. The ratio of the peak radiative and total heat fluxes at the different times attains a value of 28%.

Figure 15b depicts the effect of including the atomic spectral lines to the nonequilbrium radiation simulations. By omitting the contribution of the fine atomic spectral structure, the calculated radiative heat transfer rates underpredict both data bases over the entire reentry range. The accompanying experimental data are sorted by Johnston into the categories of coupled and uncoupled radiation with chemically reacting flows. From the specific comparison, the calculated peak heating time shifts from the measurements by three seconds, and this forward time shift has also been observed from all known computational simulations [2,3].
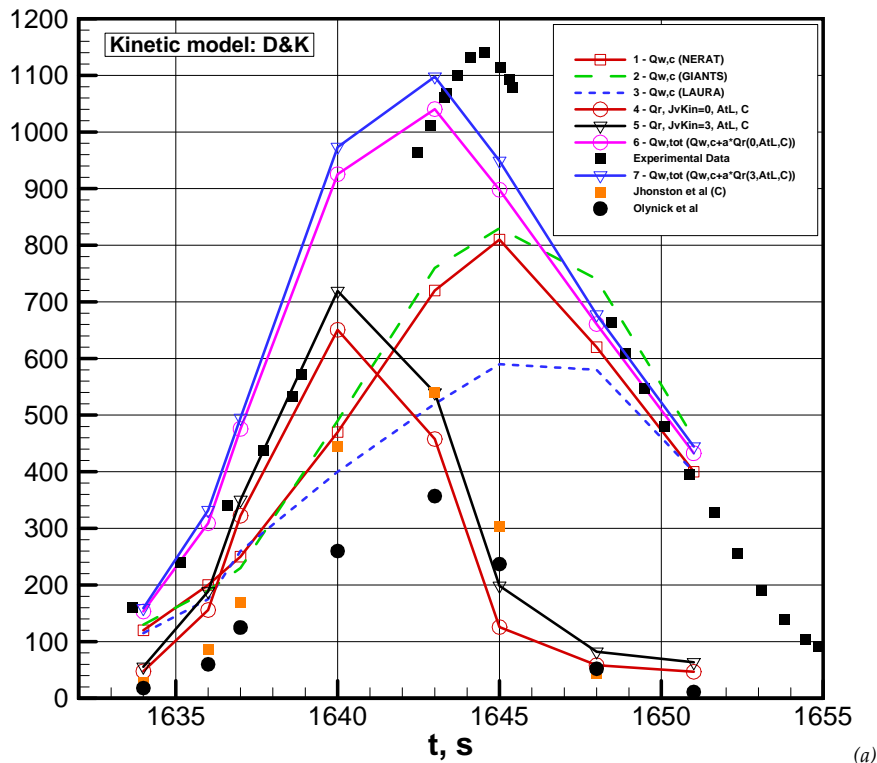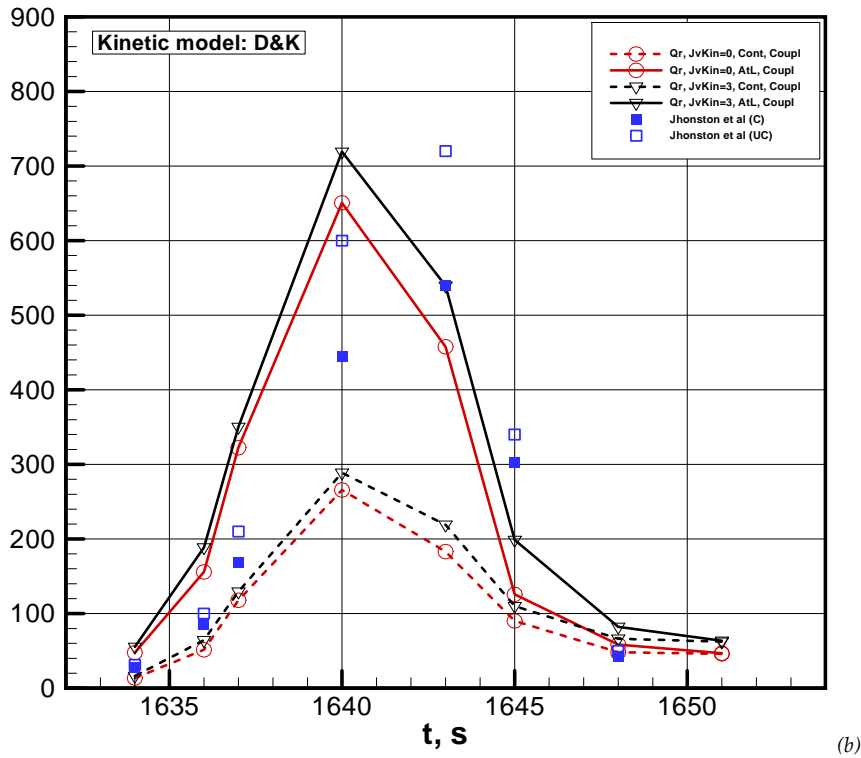

(a)

FIG. 15A. CONVECTIVE AND RADIATIVE HEATING OF STAGNATION POINT OF FIRE-II (W/CM²) WITH KINETIC MODEL [11]; CONVECTIVE HEAT FLUXES PREDICTED BY (1) NERAT (WITHOUT RADIATIVE-GASDYNAMIC INTERACTION), (2) GIANT AND (3) LAURA CODES; HEAT FLUXES PREDICTED BY (4,5) NERAT+ASTEROID CODES WITH DIFFERENT KINETICS OF DISSOCIATION; TOTAL (CONVECTIVE+RADIATIVE) HEATING, PREDICTED BY NERAT+ASTEROID CODES (6,7) (SUBSCRIPT "A" POINTS TO TAKING INTO ACCOUNT OF RADIATION ABSORPTION BY OPTICAL WINDOW OF RADIATION RECEIVER AS IT WAS MADE IN [2,3]); EXPERIMENTAL DATA BY CAUCHON, TOTAL RADIATIVE-CONVECTIVE HEATING PREDICTED BY OLYNICK ET AL , AND RADIATION HEAT FLUX BY JOHNSTON ET AL ARE SHOWN AS SEPARATE POINTS.

(b)

FIG. 15B. RADIATION HEAT FLUXES IN W/CM². RESULTS OBTAIN FOR COUPLED GASDYNAMICS-RADIATION BY NERAT+ASTEROID CODES WITH (SOLID LINES) AND OBTAINED WITHOUT ATOMIC LINES (DASHED LINES) USING DIFFERENT CHEMICAL KINETIC MODELS. RADIATION HEAT FLUXES PREDICTED WITH AND WITHOUT COUPLING ARE SHOWN BY SEPARATE POINTS; USING KINETIC MODEL [11]
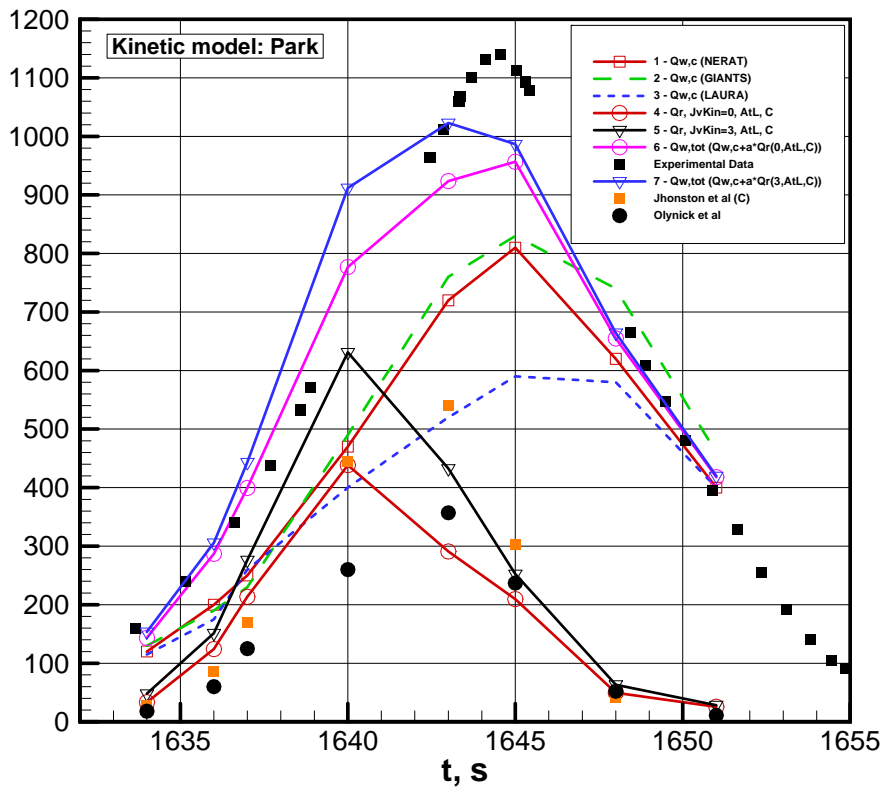

FIG. 16A. CONVECTIVE AND RADIATIVE HEATING AT STAGNATION POINT OF FIRE-II IN W/CM² USING KINETIC MODEL [12]; CONVECTIVE HEAT FLUXES PREDICTED BY (1) NERAT, (2) GIANT AND (3) LAURA [2] CODES; (4,5) – INTEGRATED RADIATION HEAT FLUXES PREDICTED BY NERAT+ASTEROID CODES WITH DIFFERENT DISSOCIATION MODELS; (6,7) –TOTAL HEATING BY NERAT +ASTEROID CODES. EXPERIMENTAL DATA BY CAUCHON [1], TOTAL HEATING PREDICTED BY OLYNICK ET AL [2], AND RADIATION HEAT FLUX BY JOHNSTON ET AL [3] ARE SHOWN BY SEPARATE POINTS
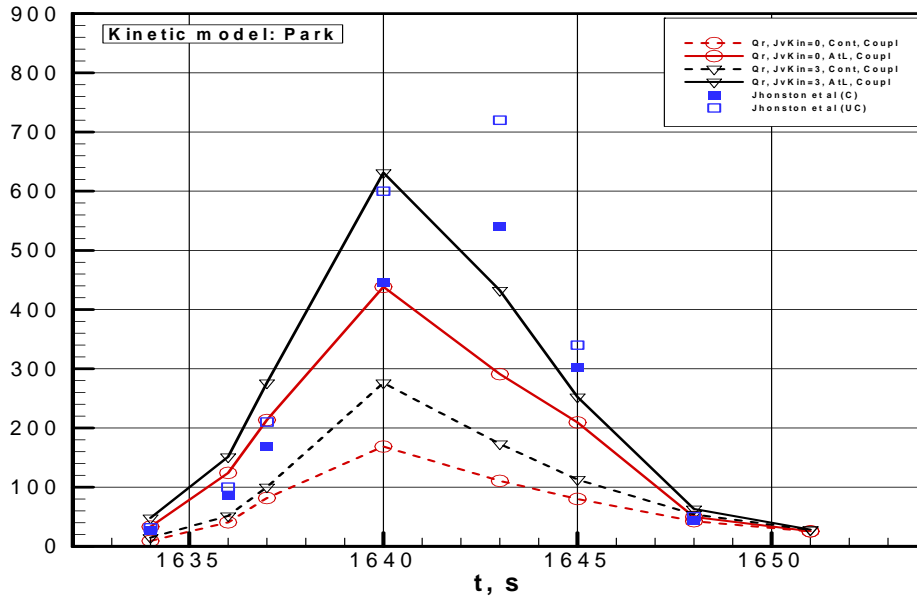
FIG. 16B. INTEGRATED RADIATION HEAT FLUXES IN W/CM², COUPLED GASDYNAMICS-RADIATION RESULTS BY NERAT+ASTEROID CODES WITH (SOLID LINES) AND WITHOUT ATOMIC LINES (DASHED LINES) USING DIFFERENT DISSOCIATION KINETIC MODELS. RADIATION HEAT FLUXES PREDICTED WITH AND WITHOUT COUPLING ARE SHOWN BY SEPARATE POINTS; KINETIC MODEL [12].

The computational results given by Figure 16a, using the basic kinetics model by Park under predict the data bases. The under-prediction has a value around 110 W/cm², or 9.6% lower than the data by Cauchon; but nearly duplicates the peak heating condition at the time frame. In other words, the discrepancy with data is 1.91 times greater than the data scattering band determined by Johnston [3]. Meanwhile, a greater difference in radiation prediction is revealed by the different nonequilibrium dissociation models. In fact, the calculated radiative fluxes by Park's model show a greater sensitivity than the model by Dunn-Kung in conjunction with the use of LTE and the Treanor-Marrone formulation. Again the numerical results of Olynick et al and correlated data by Johnston are also presented for purpose of comparison.

Figure 16b presents the radiative heat flux calculation with/without the modeling of atomic lines. Again the results of radiation display a greater sensitivity to the nonequilibrium chemical-physics kinetics models by the Park [12] than that by Dunn-Kang [11] in regards to detailed formulation of internal degrees of excitations. The numerical results for radiative heating underpredict the correlated data of coupled/uncoupled radiation with the chemical reacting flowfield. Meanwhile, the predicted time line for peak heating improves slightly with the data. In short, the present results including the atomic line spectra reach a much better agreement to these data than all other numerical simulations.

From the above comparative study by including the atomic lines to the radiative transfer calculation for the Fire II reentry, an additional heat transfer of more than 400 W/cm² is produced using the chemical kinetics model of Dunn-Kang. A lesser amount of 320 W/cm² is generated by adopting the chemical kinetics model of Park. The altered spectral property is dependent strongly on the nonequilibrium chemical-physics kinetics models. It is therefore possible to conclude that variation of different models of chemical and chemical-physics kinetics allows an improved agreement with the flight data by the radiation-gasdynamics coupling and by including the spectral lines of atoms and ions for optical property evaluation.

Figures 15b and 16b show differences between results obtained with/without atomic lines (for different kinetic models). These figures actually demonstrate differences between atomic and molecular radiation, both groups of results include continuum radiation generated by free-free (f-f) and free-bound (f-b) transitions. The detailed analysis of contribution to different radiation processes [f-f, b-f, and bound-bound (b-b)] in equilibrium conditions by spectral emissivity is presented in reference 33.

It should also be mentioned that we have considered all significant b-b, b-f and f-f transitions. The detailed information on the contribution of different radiative processes to absorptivity and emissivity of heated air, at

similar conditions, is presented in reference 30. The analysis of cumulative functions allows us to estimate contributions of different radiative processes. Figure 13 in reference 33 shows, that at wavenumber less than 10 000 1/cm *f-f* transitions and partially emissivity from excited atomic levels are dominant. The radiation emission due to atomic lines and photo-recombination are significant in the UV spectral region. In the near IR, UV and in the visible spectral regions, the electronic molecular bands are dominant.

Conclusion

The numerical simulations of aerothermodynamics and aerophysics for the reentry probe Fire-II have been performed by using the computer programs NERAT-ASTEROID. The numerical results generated by using different models of chemical and chemical-physical kinetics at the equilibrium and nonequilibrium conditions are presented.

The numerical simulations for nonequilibrium radiation heat transfer of the reentering Fire II probe based on two widely adopted nonequilibrium chemical kinetic models by Park and Dunn-Kang, are carried out with/without gasdynamic-radiative coupling. The numerical solutions to vibrational relaxation are also presented by the different assumptions of local thermodynamic equilibrium (LTE) and a dissociation biased model. The effects to the standoff distance and temperature profiles within the critically important shock layer are systematically delineated.

Most importantly, for the first time the contribution to the total heat transfer rate is demonstrated by including the spectral lines of atoms and ions for optical properties of the radiating gas. The new spectral data base developed by an *ab-initio* approach has been verified by comparison with experimental data and others computational results to show the significance of radiative heating for the reentering simulations. The new finding has remedied a long-puzzling; under-prediction deficiency of nonequilibrium radiative heat transfer rates to the Fire II Probe.

At the same time, the computational simulation for the nonequilibrium radiative heating of the spacecraft surface is still subject to wide variation through the use of different kinetics models and spectral lines of atoms and ions.

REFERENCES

[1]   Cauchon, D.L, Radiative Heating Results from the Fire II Flight Experiment at a Reentry velocity of 11.4 km/s, 1967. NASA TM-X-1402

[2]   Olynick, D.R., Henline, W.D., Hartung L.C., and Candler, G.V., Comparison of Coupled RadiativeNavier-Stokes Flow Solutions with the Project Fire-II Flight Data, AIAA 94-1955, 1994.

[3]   Johnston, C.O., Hollis, B.R., Sutton, K., Nonequilibrium Stagnation-Line Radiative Heating for Fire-II,JSR, Vol. 45, No.6, 2008, pp.1185-1195.

[4]   Surzhikov, S.T., Shang, J.S., Kinetic Models Analysis for Super-Orbital Aerophysics, AIAA Paper 08-1278. 2008. 17 p.

[5]   Shang, J.S., Surzhikov, S.T., and Yan, H., Hypersonic nonequilibrium flow simulation based on kinetics models, Frontiers in Aerospace Engineering, Vol. 1, No.1, Nov. 2012, pp.1-12.

[6]   Park, C., Nonequilibrium Hypersonic Aerothermodynamics, Willey-Interscience Publication, J. Wiley & Sons. New-York, 1990

[7]   Surzhikov S.T., Shang J.S.,Radiative and Convective Heating of ORION Space Vehicles at Earth Orbital Entries, AIAA Paper 2011-251, 2011, 22 p.

[8]   Diadkin, A., Beloshitsky, A., Shuvalov, M, and Surzhikov, S., Nonequilibriumradiativegasdynamics of segmental-conical space vehicle of large size, AIAA 2011-453, 2011, 29 p.

[9]   Shang J.S., Surzhikov S.T., Simulating Stardust Earth Reentry with Radiation Heat Transfer, JSR, Vol. 48, No.3, 2011, pp.385 396.

[10]   Surzhikov, S.T. and Shang, J.S., Coupled radiation-gasdynamic model for Stardust earth entry simulation, J. of Spacecraft and Rockets, Vol. 49, No. 5, 2012, pp.875-888.

[11]   Dunn, M.G. and Kang, S.W., Theoretical and Experimental Studies of Reentry Plasmas, NASA CR 2232, April 1973.

[12]   Park, C., Review of Chemical-Kinetics Problems of Future NASA Missions, I: Earth Entries, Journal of Thermophysics and Heat Transfer, Vol.7, No.3, 1993.

[13]   Treanor, C.E., Marrone, P.V., "Effect of Dissociation on the Rate of Vibrational Relaxation, Phys. of Fluids. 1962. Vol. 5. No. 9. pp. 1022-1026.

[14]   Surzhikov, S.T., Computing System for Mathematical Simulation of Selective Radiation Transfer, AIAA Paper № 00-2369. 2000. 15 p.

[15]   Surzhikov, S.T., Computational Radiation Models for Low-Temperature Plasma, AIAA Paper. № 96 2313. 1996. 11 p.

[16]   Sherman, M.P., Moment Methods in Radiative Transfer Problem, JQSRT. Vol.7. No.1. pp.89 109. 1967.

[17]   Millikan, R., White, D., Systematics of Vibrational Relaxation. J. of Chem. Phys. 1963. Vol.39. No.12. pp. 3209-3212.

[18]   Gurvich, L.V., Veitc, I.V., Medvedev, V.A. et al. Thermodynamic Properties of Individual Substances. Handbook. Vols.1-4. Moscow: Nauka. 1978.

[19]   Svehla, R.A., Estimated Viscosities and Thermal Conductivities of Gases at High Temperatures. NASA TR-R-132. 1962. 26 P.

[20]   Capitelli, M., Gorse, C., Longo, S., Giordano, D., Collision Integrals of High-Temperature Air Species. Journal of Thermophysics and Heat Transfer. 2000. Vol.14. No. 2. P.259 268.

[21]   Levin, E., Wright, M.J., Collision Integrals for Ion-Neutral Interactions of Nitrogen and Oxygen. Journal of Thermophysics and Heat Transfer. 2004. Vol.18. No.1. P.143 147.

[22]   Wilke, C.R., Diffusional Properties of Multicomponent Gases. Chem. Engn. Progr. 1950. Vol.46. p. 95-104.

[23]   Bird R., Stewart W., Lightfoot E., Transport Phenomena. John Wiley & Sons. Inc. 1965.

[24]   Surzhikov, S.T., Data Base of Atomic Lines for Radiative Gas Dynamic Models, AIAA Paper № 02-2898. 2002.

[25]   Bates, D.R., Damgaard, A., The calculation of absolute strengths of spectral lines, Phil. Trans. Roy. Soc., 1949, Vol.242, p.101-111

[26]   Hartree, D.R., The Calculation of Atomic Structures, John Wiley & Sons, Inc., New York, 1957

[27]   Moore, C.E., Atomic energy levels, NBS Circular 467, Washington D.C., Vol.1, 1949; Vol.2, 1952; Vol.3, 1958. See also NIST data base.

[28]   Dikalyuk, A.S., Surzhikov, S.T., Kozlov, P.V., Shatalov, O.P. and Romanenko, Yu.V., Nonequilibrium Spectral Radiation behind the Shock Waves in Martian and Earth Atmospheres. AIAA paper-2013-2505. 44th AIAA Thermophysics Conference, June 24-27, 2013, San Diego, CA.

[29]   Sobelman, I.I., Atomic spectra and radiative transitions, 2nd Edition

[30]   Springer. 1992. ISBN: 3540545182. 373 pages.

[31]   Griem, H.R., Plasma Spectroscopy, McGraw-Hill, New York, 1964.

[32]   Surzhikov, S.T., Radiative-Collisional Models in Non-Equilibrium Aerothermodynamics of Entry Probes. Journal of Heat Transfer. March 2012. Vol.134. 031002-1-11

[33]   Surzhikov, S.T., Omaly P. Radiative Gas Dynamics of Martian Space Vehicles. AIAA paper 2011- 0452. 2011.

[34]   Surzhikov, S.T., Application of quantum mechanics and quasi-classical models of elementary processes in high temperature gases for computational models of entry probes aero physics. Proceedings of the 7th European Symposium on Aerothermodynamics, 9-12 May 2011, Brugge, Belgium.